Visualizing nuclear pore complex plasticity with Pan-Expansion Microscopy

Kimberly J. Morgan[1], Emma Carley[1], Alyssa N. Coyne[2, 3], Jeffrey D. Rothstein[2, 3], C. Patrick Lusk*[1], Megan C. King*[1, 4]

[1]Department of Cell Biology, Yale School of Medicine, New Haven, CT, 06520, USA.

[2]Brain Science Institute, Johns Hopkins University School of Medicine, Baltimore, MD, 21205, USA.

[3]Department of Neurology, Johns Hopkins University, Baltimore, MD, 21205, USA.

[4]Department of Molecular, Cell and Developmental Biology, Yale University, New Haven, CT, 06520, USA.

*Correspondence:
patrick.lusk@yale.edu
megan.king@yale.edu

Abstract

Cell-type specific and environmentally-responsive plasticity in nuclear pore complex (NPC) composition and structure is an emerging area of investigation, but its molecular underpinnings remain ill defined. To understand the cause and consequence of NPC plasticity requires technologies to visualize differences within individual NPCs across the thousands in a given nucleus. We evaluate the utility of Pan Expansion Microscopy (Pan-ExM), which enables 16-20 fold isotropic cell enlargement while preserving the proteome, to reveal NPC plasticity. NPCs are robustly identified by deep learning-facilitated segmentation as tripartite structures corresponding to the nucleoplasmic ring, inner ring with central transport channel, and cytoplasmic ring, as confirmed by immunostaining. We demonstrate a range of NPC diameters with a bias for dilated NPCs at the basal nuclear surface, often in local clusters. These diameter biases are eliminated by disrupting linker of nucleoskeleton and cytoskeleton (LINC) complex-dependent connections between the nuclear envelope (NE) and the cytoskeleton, supporting that they reflect local variations in NE tension. Pan-ExM further reveals that the transmembrane nucleoporin/nup POM121 resides specifically at the nuclear ring in multiple model cell lines, surprising given the expectation that it would be a component of the inner ring like other transmembrane nups. Remarkably, however, POM121 shifts from the nuclear ring to the inner ring specifically in aged induced pluripotent stem cell derived neurons (iPSNs) from a patient with *C9orf72* amyotrophic lateral sclerosis (ALS). Thus, Pan-ExM allows the visualization of changes in NPC architecture that may underlie early steps in an ALS pathomechanism. Taken together, Pan-ExM is a powerful and accessible tool to visualize NPC plasticity in physiological and pathological contexts at single NPC resolution.

Introduction

The nuclear envelope (NE) is a double membrane barrier that segregates the nuclear genome from the cytoplasm. Bidirectional molecular communication across the NE is mediated by nuclear pore complexes (NPCs), protein gateways that facilitate the selective transport of cargo-bound nuclear transport receptors (NTRs) while also imposing a size-restrictive diffusion barrier. It is well understood how the majority of the key building blocks (nucleoporins or nups) are arranged to build the iconic 8-fold radial architecture of the NPC with recent cryo-EM and cryo-ET structures approaching atomic resolution (Akey et al., 2023; Akey et al., 2022; Bley et al., 2022; Fontana et al., 2022; Huang et al., 2022a; Huang et al., 2022b; Kosinski et al., 2016; Mosalaganti et al., 2022; Petrovic et al., 2022; Schuller et al., 2021; Singh et al., 2024; von Appen et al., 2015; Zhu et al., 2022). These studies have provided a blueprint for the NPC in multiple organisms, glimpses of its evolutionary history and key insights into its assembly and function. They have also revealed that the NPC structure is not monolithic. Indeed, there are numerous hints that NPCs are surprisingly plastic in composition and structure, but the causes and consequences of this likely plasticity are just beginning to come to light (Fernandez-Martinez and Rout, 2021). A key challenge for the field is to be able to directly visualize this plasticity on a single NPC level.

The recent discoveries that the NPC scaffold is dilated *in cellulo* compared to in isolated NEs and can constrict in response to energy depletion or hyperosmotic shock suggest that lateral strain on NPCs imposed by NE tension could modulate NPC architecture and function (Akey et al., 2022; Mosalaganti et al., 2022; Schuller et al., 2021; Zimmerli et al., 2021). It remains unknown, however, whether changing the diameter of NPCs impacts their selective permeability (although there is emerging evidence that supports this concept)(Elosegui-Artola et al., 2017; Feng et al., 2024; Klughammer et al., 2024; Kozai et al., 2023). Further, it is unclear whether NPC diameter is controlled by passive mechanisms or whether it can be actively modulated, perhaps even in response to the local NE environment. Considering the latter, it is plausible that mechanotransduction mechanisms that translate extracellular mechanical cues to the NE through Linker of Nucleoskeleton and Cytoskeleton (LINC) complexes may locally alter NE tension and NPC dilation. Consistent with this possibility, there is evidence that mechanical strain on the

nuclear lamina is higher at the basal versus apical surface of the nucleus (Carley et al., 2021; Ihalainen et al., 2015). Whether this asymmetry in lamina tension is reflected in the dilatory state of NPCs is unknown. Answering these questions will require facile and accessible methods to examine NPC diameter, ideally at single NPC resolution, in multiple cell types and tissues.

Similar methods are also required to tackle the question of whether NPCs are compositionally (and functionally) different among cell types in both physiological and pathological settings (Cho and Hetzer, 2020; Fernandez-Martinez and Rout, 2021). For example, it has been reported that there are at least two forms of NPCs in budding yeast with either one or two nuclear rings (Akey et al., 2022). Moreover, the nuclear basket is absent from many yeast NPCs and may be assembled as part of a dynamic mRNA export platform (Bensidoun et al., 2022; Galy et al., 2004; Singh et al., 2024). Whether there is such plasticity of the nuclear basket in human cells remains unknown, but there are many hints that there is compositional heterogeneity of NPCs in certain cell types driven by differential nup expression and/or turnover rates, both of which may be influenced by age and disease (Cho and Hetzer, 2020). Importantly, although cryo-ET may be amenable to uncovering broad classes of NPC structures in scenarios where there is a total absence of a given nup, it will be less valuable in cases where there may be changes in the relative stoichiometry of nups within individual NPCs.

Another motivation for developing methods to visualize compositional heterogeneity at the individual NPC level is exemplified by evidence that NPCs may be compromised in neurodegenerative disease (Chandra and Lusk, 2022). Specifically, an amyotrophic lateral sclerosis (ALS) pathomechanism caused by a hexanucleotide repeat expansion in the *C9orf72* gene has been proposed to occur through an NPC injury cascade resulting in the loss of a specific subset of nups from a fraction of NPCs (Coyne et al., 2020). POM121, one of three transmembrane nups, is a key linchpin whose disappearance precedes that of other nups that ultimately herald a loss of nuclear compartmentalization (Baskerville et al., 2024; Coyne et al., 2021). The underlying mechanisms that drive these changes to NPCs remains uncertain but would clearly benefit from a methodology that can reveal the molecular and morphological changes that occur within individual NPCs along the NPC injury

cascade. Moreover, the ideal method would couple quantitative immunolabeling with the capacity to assess gross changes in NPC architecture.

Here, we explore the utility of Pan Expansion Microscopy (Pan-ExM) to robustly visualize the molecular composition and structure of individual NPCs. Pan-ExM is unique over other expansion microscopy methods as it preserves the total proteome, which can be visualized at an ultrastructural resolution using a “pan” fluorescent protein stain (M'Saad and Bewersdorf, 2020). We demonstrate that machine-learning based segmentation of Pan-ExM images can robustly and comprehensively identify individual NPCs. Not only can Pan-ExM reveal the compositional heterogeneity of NPCs on an individual NPC level but it can also reveal local differences in NPC diameter tied to cell polarity that depend on LINC complexes. Further, we used Pan-ExM to make the unexpected discovery that, unlike the other transmembrane nups, POM121 is asymmetrically distributed to the nuclear ring. Most remarkably, although POM121’s nuclear ring localization is observed across several human cell lines, in induced pluripotent stem cell derived neurons (iPSNs) from a patient with the pathological *C9orf72* repeat expansion, we observed a shift in the distribution of POM121 from the nuclear ring to the inner ring that we tie to further loss of NPC density as revealed by the pan-stain. These data suggest that discrete changes to NPC architecture in the *C9orf72* ALS NPC injury cascade that were previously unappreciated are visible by Pan-ExM. Thus Pan-ExM is a valuable discovery tool that will help illuminate NPC plasticity – an essential step towards understanding its function across cells and tissues.

Results

Pan-ExM permits visualization of whole cell proteinaceous ultrastructure including NPCs.

To visualize cellular ultrastructure and NPCs, we leveraged the Pan ExM (M'Saad and Bewersdorf, 2020) protocol and fixed and embedded samples in a series of swellable hydrogels, enabling ~16-fold expansion (Supplementary Figure 1). A schematic of the procedures and computational tools used in this study are diagrammed in Figure 1. Briefly, to “pan” stain all cellular proteins, lysines across the proteome were labeled with a fluorophore conjugated N-Hydroxysuccinimide (NHS), DNA was labeled with SYTOX Green and proteins of interest were labeled with antibodies (Figure 1a). Using confocal microscopy, we acquired images capturing whole cell volumes. As expected (M'Saad and Bewersdorf, 2020), cellular organelles like nucleoli, mitochondria, Golgi stacks and centrioles were identifiable by their characteristic ultrastructural morphologies revealed by the pan-stain (Figure 1b). NPCs were likewise visible at the edge of the nucleus (Figure 1b). We developed an image analysis pipeline using Imaris software and the Fiji (Schindelin et al., 2012) plugin LABKIT (Arzt et al., 2022), a machine-learning based random forest classifier, to segment cellular structures in 3D (Figure 1c). Through manual labeling of image voxels in all acquired channels, nuclei were segmented by iterative training. NPCs were robustly identified in all axial orientations and automatically segmented by training multiple datasets. To measure NPC diameter required training a different classifier to accurately segment the nuclear ring of NPCs. This analysis was further combined with segmentation of antibody labeling and annulate lamellae (AL). Together, these in silico segmentation approaches enable a detailed ultrastructural analysis of all NPCs in a given cell nucleus in virtually any cell line. Initially, we examined three commonly used cell lines: HeLa cervical adenocarcinoma, A549 lung adenocarcinoma and SH-SY5Y neuroblastoma cells.

In axial sections of magnified views of the nuclear surface, each NPC (regardless of cell line) was comprised of a single focus suspended between two rings (Figure 2a). The former is best observed in cross section (Figure 2b). Consistent with a body of prior work (Krull et al., 2010; M'Saad and Bewersdorf, 2020; Ou et al., 2017; Schermelleh et al., 2008) supporting that NPCs engage euchromatin and/or exclude heterochromatin, the nuclear rings were nestled within islands lacking detectable

SYTOX fluorescence (Figure 2a, bottom panels). A quantitative comparison of the average NPC architecture derived from 2061 NPCs in Pan-ExM samples with those derived from *in cellulo* cryo-ET of human NPCs (Mosalaganti et al., 2022; Schuller et al., 2021) indicates that Pan-ExM results in expansion of the NPC ~2 fold more along the nuclear transport axis compared to the radial axis (Supplementary Figure 2a). Indeed, comparing the relative dimensions observed in the expanded NPCs to the average cryo-ET structure of NPCs in intact DLD-1 cell nuclei (Schuller et al., 2021) supports that Pan-ExM maintains a faithful relationship between the diameter of the nuclear and inner rings (Supplementary Figure 2b, c). Moreover, we can also discern that the inner ring is more proximal to the nuclear ring than the cytoplasmic ring, a prominent feature of the DLD-1 NPC model (Schuller et al., 2021) (Supplementary Figure 2a, b, d). However, the dimensions along the nuclear transport axis are exaggerated (Supplementary Figure 2a). Regardless, NPCs and their substructure are easily visualized by Pan-ExM with the relative dimensions of the nuclear, inner and cytoplasmic rings preserved.

The ability to segment NPCs and nuclear contours provided a facile approach to automate counting all the NPCs of hundreds of HeLa, A549 and SH-SY5Y nuclei and to correlate these values to nuclear surface and volume measurements. The latter were normalized to an expansion factor calculated for each sample by measuring the mean distance between the membranes of mitochondria cristae (Supplementary Figure 1a) and centriole diameters (Supplementary Figure 1b); the average of these two was then taken as the expansion factor for assigning pre-expansion scale (Supplementary Figure 1c). There was remarkable consistency in sample-to-sample expansion that ranged from 13.94 to 16.69 fold (Supplementary Figure 1d). On average, the three cell lines had a similar mean number of NPCs with considerable variability on an individual cell basis. HeLa cells displayed the largest spread in values (over 7-fold) and SH-SY5Y cells, the least (Figure 2c). As such, SH-SY5Y cells also had the highest density of NPCs that were closest to each other (Figure 2d,e). To gain some insight into the mechanisms that may influence NPC number, we further related NPC number to the nuclear surface area and nuclear volume on an individual cell basis. Across all cells examined, NPC number was correlated with nuclear surface area (Figure 2e-h) and nuclear volume (Figure 2i-l),

with modestly stronger correlations with nuclear volume. Thus, Pan-ExM is a valuable and facile approach to count NPCs in relation to nuclear metrics.

Local differences in NPC dimensions

Emerging work has intimated that the NPC diameter adopts a range of dilation states in response to NE tension, which in turn may be modulated by both cell-intrinsic and extrinsic factors (Mosalaganti et al., 2022; Schuller et al., 2021; Zimmerli et al., 2021). Although an exciting concept, we know little about the factors that govern if NPCs in a single nucleus exist in different dilatory states and, if so, if this is biologically meaningful. While the most pronounced quantitative changes in NPC diameter when comparing a no tension state (isolated NEs) and a physiological tension state (*in cellulo*) manifest at the inner ring, which expands ~30% in two different cryo-ET models of human cells (Mosalaganti et al., 2022; Schuller et al., 2021), changes in tension are also reflected in the pore membrane to pore membrane distance (a 12-18% expansion in human cells (Mosalaganti et al., 2022; Schuller et al., 2021). The effect of NE tension on the dilation of the nuclear and cytoplasmic rings is more modest and most clearly revealed by comparing fission yeast NPC cryo-ET structures in different NE tension states – here a 13% change in the nuclear ring diameter was observed (Zimmerli et al., 2021). It is important to note, however, that the cryo-ET models are all averaged structures, and the inner ring diameter of individual NPCs in cryo-ET preparations varies remarkably (Schuller et al., 2021; Zimmerli et al., 2021). To test whether Pan-ExM could provide a tool to readily evaluate relative NPC diameter within individual cells at high sampling density, we measured the diameters of thousands of nuclear rings of computationally segmented NPCs on a given HeLa nucleus as this element of the NPC allowed for the most robust measurements. In line with prior observations (Schuller et al., 2021), we likewise noted that there was a near two-fold range in NPC diameter values across the nucleus (Figure 3a). Leveraging our ability to comprehensively assess all NPCs, we further investigated whether shifts in this range are likely to reflect bona fide local NPC diameter differences. To that end we compared the diameters of NPCs on the top and bottom of the nucleus; there is evidence that tension on the nuclear lamina is higher on the bottom of the nucleus due to cell adhesion to the extracellular matrix (Carley et al., 2021; Ihalainen et al., 2015). Consistent with the expectation that higher force transduction to the nuclear lamina increases NE

tension in a way that could enhance NPC dilation, we observed a significant trend of larger NPC diameters on the basal surface of the nucleus compared to the apical surface, although there is a marked variance across the NPC population on both surfaces (Figure 3a). This NPC diameter bias between the basal and apical aspects of the nucleus was mirrored in both A549 and SH-SY5Y cells (Figure 3d; Supplementary Figure 3), supporting that this is a general phenomenon. One interpretation of these data is that there are localized regions of high NE tension, particularly on the basal nuclear surface.

Interestingly, when we binned the NPC diameters into quintiles, the distance to the five nearest NPCs in the same diameter class was shortest for NPCs with the largest 20% of diameters (Figure 3b). Indeed, compared to a randomly selected 20%, middle 20% or to the smallest 20%, the largest NPCs were significantly closer together. Color-coding of NPCs at the basal nuclear surface according to NPC diameter class revealed that larger NPCs appeared to locally cluster in apparent hot spots (Figure 3c, purple). These results were mirrored in A549 cells (Figure 3e, f). Thus, a generalizable principle appears that the largest NPCs cluster together in local regions across the nuclear surface.

To investigate whether the measured biases in NPC diameter reflected the functional integration of NPCs within a mechanoresponsive network (and to rule out expansion-induced artifacts), we performed Pan-ExM and measured NPC diameters in CRISPR-edited A549 cells lacking *Sun1* and *Sun2* (Supplementary Figure 4). SUN1 and SUN2 are integral components of LINC complexes (Chang et al., 2015) necessary to transmit cytoskeletal forces from cell-matrix adhesions to the nuclear lamina (Carley et al., 2021). Strikingly, the ablation of LINC complexes completely disrupted the observed bias for larger NPC diameters on the basal surface of the nucleus (Figure 3g), which were now also found to be uniformly distributed (Figure 3i). Indeed, we no longer detected a bias for the largest NPCs to cluster (Figure 3h, i). Thus, Pan-ExM can detect LINC-complex dependent changes in relative NPC diameter within single nuclei while also providing evidence for a putative mechanoresponsive response that has yet to be directly documented.

Last, the modest magnitude of the shift in the mean nuclear ring diameter at the top and bottom of the nucleus in the Pan-ExM samples is in line with the expectation that it is far less susceptible to tension-induced dilation than the inner ring. In addition, even in the context of LINC complex ablation, there is likely remaining tension on the NE driven by other mechanisms (e.g. compressive actomyosin networks or colloidal osmotic pressure) that may prevent the complete relaxation of NPCs. We therefore investigated the diameters of NPCs in Pan-ExM samples within annulate lamellae (AL), stacks of ER sheets filled with NPCs that would not be predicted to be under tension. Consistent with this idea, the NPC diameter in AL was markedly (35%) reduced compared to NPCs at the NE (Figure 3a). When taken together, our findings reinforce that Pan-ExM can reveal the conformation of individual NPCs and is therefore an invaluable approach for detecting a range of relative NPC diameters that could reflect distinct NPC states. Moreover, our observations suggest that while LINC complex-dependent tension states at the NE can meaningfully influence NPC diameter, this quantitative effect remains only a fraction of the variance in NPC diameters that are observed even within the same nucleus.

Nup antibody labeling defines NPC ultrastructure in Pan-ExM

We next assessed whether individual nups could be localized within the Pan-ExM ultrastructure by immunostaining of expanded cells with a battery of nup specific antibodies. We tested antibodies directed against nups representative of all major NPC architectural elements (Figure 4a, Supplementary Figure 5) including the cytoplasmic and nucleoplasmic rings, the inner ring, the FG-rich central channel, the nuclear basket, and the cytoplasmic filaments (Figure 4b). The anti-nup antibodies specifically labeled one or more of the three substructures of the expanded NPCs in a manner congruent with their established locations. For example, we observed anti-NUP107 staining at both pan-stained rings confirming these to be the cytoplasmic and nucleoplasmic rings (Figure 4a-c). By contrast, the pan-stained focus suspended between the two rings was recognized by antibodies to the central channel FG-nups NUP62 and NUP98, the inner ring component, NUP93, and the integral membrane nucleoporins NDC1 and GP210. Thus, this middle focus represents the inner ring with FG-network. Last, although the position of the nuclear basket (NUP50, NUP153, TPR) and cytoplasmic filament (NUP358) labels also converged qualitatively on the pan-stained cytoplasmic and nucleoplasmic rings, quantification of the label position

relative to the SYTOX stain (after normalization to the position of NUP107 to define the “middle” of the NPC) supports that they do, as expected, extend away from the rings into the nucleoplasm and cytoplasm, respectively (Figure 4c). Thus, the overall position of nups within the NPC architecture is retained during fixation and expansion of NPCs.

As the pan-stain identifies all NPCs and major architectural units, a major advantage of this approach is the ability to directly assess antibody labeling efficiency – a necessity to unambiguously detect potential changes in nup composition at the individual NPC level. For the central channel FG-nups and the scaffold elements of the NPC including the cytoplasmic, nucleoplasmic and inner rings, we observed specific and near-comprehensive labeling of the pan-stained NPCs (Figure 4d). In contrast, the labeling of the nuclear basket nups NUP50, TPR and NUP153 and the cytoplasmic filament nup Nup358 was notably less efficient (64-82%). Thus, it is possible there are sub populations of NPCs that lack these asymmetric elements, in line with observations in budding yeast that the presence of the nuclear basket reflects an mRNA export state (Bensidoun et al., 2022).

Pan-ExM reveals organization of NPCs in AL

We next assessed whether Pan-ExM could be used to provide insight into the composition and 3D organization of AL, which were robustly observed in an iPSC line and were occasionally present in HeLa and SH-SY5Y cells. As expected from prior EM studies (Cordes et al., 1996; Kessel, 1983), the NPCs in AL were organized in densely stacked arrays that we present in both an en face (top-down; Figure 5a) and lateral (Figure 5b) orientations. While EM favors efficient labeling of membranes, we expected that the total protein labeling in Pan-ExM could provide new insight into putative interactions between NPCs that may underlie the biogenesis of AL. Indeed, the outer rings of the NPCs appeared to directly connect to NPCs both above and below in two conformations (Figure 5c). In one, the NPCs were stacked on top of each other such that the transport channels aligned. In another, the NPCs were offset in a brick-like pattern. Most AL comprised a mixture of these two arrangements. In principle, the observed juxtapositions of NPCs could be driven by interactions between asymmetric elements of NPCs i.e. the cytoplasmic filaments and nuclear basket, or between symmetric elements (i.e. the outer rings).

To test these models of NPC stacking in AL, we immunolabeled cells with nup antibodies (Figure 5d). Whereas antibodies directed towards the FG-nups, NUP62 and NUP98, robustly labeled AL, we only observed sparse labeling of the cytoplasmic filament nup NUP358 and, surprisingly, the transmembrane nups POM121, NDC1 and GP210. We were unable to identify the basket component NUP153 in AL stacks, despite clear NUP153 staining at NPCs embedded in the NE in the same expanded cell. Thus, our observations, when taken together with other studies including proteomic analyses of AL from *Drosophila* embryos (Hampoelz et al., 2016; Hampoelz et al., 2019; Rasala et al., 2008; Walther et al., 2003), support that NPCs in AL have reduced levels of transmembrane nups and lack the asymmetric elements of the NPC. Thus, we favor the hypothesis that direct outer ring interactions facilitate the NPC stacking underlying AL formation.

POM121 localizes specifically to the nuclear ring

Given our surprising observation that antibodies to transmembrane nups poorly label AL (Figure 5d) despite efficiently labeling NPCs embedded in the NE (Figure 4d), we were prompted to take a closer examination of their position in NPCs by Pan-ExM. Indeed, although we understand the position of virtually all soluble nups within the NPC, there remains uncertainty over the distribution of the pore membrane proteins, particularly POM121. POM121 is not observed in cryo-EM maps despite strong *in vitro* evidence suggesting that it is capable of biochemically interacting with components of both the inner and outer rings (Yavuz et al., 2010), perhaps in a mutually exclusive manner (Mitchell et al., 2010). Thus, in principle we would expect that POM121 could localize to either the inner or outer rings (or both). We therefore used Pan-ExM to test the distribution of POM121 by immunolabeling of expanded HeLa cells. Interestingly, unlike antibodies directed to the other transmembrane domain-containing nups, GP210 and NDC1, which stained the inner ring (Figure 4), POM121 antibodies exclusively labeled the nuclear aspect of the NPC (Figure 6). This surprising result was not unique to HeLa NPCs, as we observed the identical asymmetry in the POM121 labeling of A549 and SH-SY5Y cells (Figure 6a, c). Importantly, labeling of POM121 at this biased position was equally efficient as the other pore membrane nups (compare Figure 6b and Figure 4d), suggesting the robustness of this observation. Moreover, the favored position of POM121 labeling

(Figure 6c) most closely mimics the position of the nuclear ring staining of NUP107 (Figure 4c). Thus, POM121 is unique amongst the transmembrane nups and is asymmetrically distributed in the NPC on the nuclear ring.

POM121 shifts position in model ALS iPSNs

To further push the boundaries of Pan-ExM and to investigate the potential functional significance of POM121's specific localization to the nuclear ring, we tested whether Pan-ExM could distinguish compositionally unique NPCs in the context of a neurodegenerative disease model. Recent work supports that there is an NPC injury cascade in which POM121 plays a critical role in the characteristic loss of a subset of nups from NEs in iPSC derived neurons (iPSNs) from patients expressing a hexanucleotide repeat expansion in *C9orf72,* the most common genetic cause of ALS (Coyne et al., 2020). The observed NPC injury occurs approximately 32 days after differentiation into motor neurons in culture. We therefore prepared differentiated iPSNs at day 18 (before NPC injury) and day 32 (after NPC injury) post-differentiation for examination by Pan-ExM. In all samples, NPCs were readily visible in the pan-stain. Notably, while the extent of immunolabeling of NUP62 (previously found to be unaffected in this disease model (Coyne et al., 2021; Coyne et al., 2020)) showed no change between day 18 and day 32 iPSNs (Supplementary Figure 6), we observed a marked reduction in the labeling of POM121 (Figure 7a, b) from 92% of NPCs at day 18 to 73% at day 32 specifically in *C9orf72* HRE-expressing iPSNs but not the WT iPSN matched control. Prior studies have suggested that loss of POM121 is a hallmark of a broader disruption in NPC composition including diminished levels of seven other nups across multiple subcomplexes (Coyne et al., 2020). Consistent with this, we also observed that NPCs lacking POM121 have a statistically significant decrease in pan-labeling within the segmented NPCs compared to POM121-containing NPCs in the same nucleus (Figure 7c). Thus, Pan-ExM allows the visualization of pathological changes to the biochemical identity of individual NPCs.

Most strikingly, upon close inspection of the anti-POM121 staining in the day 32 *C9orf72* HRE-expressing iPSNs, it was clear that in NPCs that retained POM121 it was no longer distributed along the nuclear ring (Figure 7a, bottom right panel). Indeed, in virtually all the antibody-labeled NPCs, the POM121 stain was now

mispositioned instead to the inner ring while the anti-POM121 labeling in WT iPSN controls at the same timepoint retained the normal localization at the nuclear ring (Figure 7a, d). Thus, using Pan-ExM we have visualized a remarkable response in the position of a key transmembrane nup from the nuclear ring to the inner ring in a pathological condition. While the underlying mechanism driving these changes remains uncertain, we suggest that this may be an important, but to this point invisible, step along the NPC injury cascade that may contribute to an ALS pathomechanism.

Discussion

We have investigated the ability of Pan-ExM to serve as an enabling tool for exploring several pressing questions in the nuclear transport field. We suggest that Pan-ExM fills an important niche between cryo-EM/ET and super-resolution microscopy. The Pan-ExM approach overcomes the significant financial, technical and intellectual resources required for cryo-EM/ET while also circumventing the modality-specific limitations of super-resolution imaging that are compounded by the need to access specialized microscopes. Pan-ExM particularly excels at providing insight into the molecular composition and structure (at tens of nanometer resolution) at the level of individual NPCs in a given nucleus. As it is possible to perform Pan-ExM on virtually any cell type and, with protocol modifications, tissues (M'Saad and Bewersdorf, 2020; M’Saad et al., 2022), it promises to reveal a broad spectrum of NPC diversity that has previously gone underappreciated. The ability to confidently visualize NPCs of unique molecular composition and structure, as demonstrated here, is the first step to understanding their function in both physiological and pathological contexts.

As an example of a pathological context in which Pan-ExM was illuminating, we investigated how NPCs change in an iPSN model of *C9orf72* ALS. The data first reinforce that Pan-ExM can be used to assess the presence/absence of individual nups from single NPCs, recapitulating the observed loss of POM121 during a *C9orf72* HRE-specific NPC injury cascade thought to be central to an ALS pathomechanism (Coyne and Rothstein, 2021; Coyne et al., 2020). While making a definitive conclusion from negative data (i.e. lack of immunolabeling) is always fraught, Pan-ExM has several key advantages over classic immunofluorescence and

super-resolution approaches that allows one to arrive at more confident conclusions. First, the pan-stain recognizes virtually all NPCs. This provides a facile and quantitative approach to establish the labeling efficiency per NPC for a given antibody in a manner that is challenging or impossible for other methods. Labeling efficiency is also greatly enhanced by expansion itself, overcoming epitope masking that can occur in crowded macromolecular structures and facilitating efficient penetration of antibodies into the sample (M'Saad and Bewersdorf, 2020). Indeed, we observed that the tested antibodies recognizing scaffold nups label virtually all NPCs (Figure 4d). Second, Pan-ExM revealed a remarkable change to the nanoscale distribution of POM121 that occurred specifically in the *C9orf72* HRE-expressing iPSN line 32 days after differentiation into motor neurons (Figure 7). The timing is remarkable: precisely when NPC injury has been described to begin, we observe that POM121 shifts position from the nuclear ring to the inner ring. We suspect that this change precedes the complete loss of POM121 from NPCs (Figure 7b), at which time we observe a decrease in the total bulk protein at the NPC (Figure 7c). Thus Pan-ExM revealed a new step in the NPC injury pathway; moreover, this finding suggests that there are changes in biochemical interactions among nups that likely precedes their loss from the NPC. This work thus also reveals an aspect of NPC plasticity that was previously unappreciated.

The underlying mechanism driving the shift in POM121 distribution remains unknown, but as there is evidence that POM121 can biochemically engage with both NUP160 and NUP155 in a mutually exclusive fashion (Mitchell et al., 2010), it is attractive to consider the hypothesis that POM121 moves from a NUP160-bound state (at the nuclear ring) to a NUP155-bound state (at the inner ring). While there are many plausible mechanisms that may contribute to such a change including putative post-translational modifications (Nino et al., 2016), another possibility is that POM121's location reflects its engagement with nuclear transport receptors (NTRs). POM121 is unique among the integral membrane nucleoporins in that it engages directly with the Kap α/Kap β1 NTR complex through a nuclear localization signal in its N-terminus (Rasala et al., 2008; Yavuz et al., 2010). This NLS is thought to be a key functional element that helps to target it to the inner nuclear membrane during early steps of NPC biogenesis (Funakoshi et al., 2011; Talamas and Hetzer, 2011). Interestingly, a previous study indicates that under conditions where POM121 binds

Kap α/Kap β1 it displays strong binding to NUP155 but not NUP160 (Yavuz et al., 2010). The release of Kap α binding occurs at the nuclear basket, predominantly through a mechanism requiring NUP50; the NUP50 orthologue in budding yeast, Nup2, is also essential for NLS-dependent targeting of integral membrane proteins to the inner nuclear membrane (King et al., 2006; Lokareddy et al., 2015). Interestingly, loss of NUP50 appears to be a critical component of NPC injury in ALS (Freibaum et al., 2015; Megat et al., 2023). Thus, it is plausible that the unexpected and surprising steady-state association of POM121 with the nuclear ring in model mammalian cell lines is tied to disrupted release of Kap α and a preference for binding to NUP155. This and the ultimate function of POM121 at the nuclear ring will be topics of future work that will be supported by the unique ability of Pan-ExM to reveal positional information of POM121 and other nups at the nanoscale.

While our discovery of biased positioning of POM121 at the nuclear ring of the NPC was entirely unexpected, the ability of Pan-ExM to reveal a range of NPC diameters across the same nucleus fills a critical need in the field. Indeed, approaches are needed to interrogate the contexts and consequences of NE tension on NPC form and function. Changes in NPC diameter have been proposed for decades, but only recently with “in cellulo” cryo-ET of NPC structures has definitive evidence supporting this type of NPC plasticity come to light (Akey et al., 2022; Mosalaganti et al., 2022; Schuller et al., 2021; Zimmerli et al., 2021). Here, we provide a more nuanced view of NPC diameter that supports that there is a spectrum of NPC dilatory states with a bias for the most dilated NPCs to be on the basal nuclear surface. The data further suggest that there are local islands (hundreds of square nanometers in dimensions) of NPCs that are more or less dilated. As both the local islands and basal bias of dilated NPCs are abolished upon ablation of LINC complexes, it is most likely that NE tension, driven at least in part by cytoskeletal forces, can in fact modulate NPC diameter. Such an idea may provide a function for the long-observed association of SUN1 with NPCs (Liu et al., 2007; Talamas and Hetzer, 2011), and may suggest a direct mechanoresponsive mechanism to dilate or constrict NPCs. Although the idea that NE tension may impact NPC dilation has been proposed (Elosegui-Artola et al., 2017; Mosalaganti et al., 2022; Schuller et al., 2021; Zimmerli et al., 2021), this work reveals an additional nuance: that this tension may be much more localized than previously thought. It remains mysterious, however, whether

these local NE tension differences can manifest actual functional changes to these NPCs in their ability, for example, to establish a selective transport channel and/or impact genome function, particularly as the relative mean changes in NPC diameter at the NE in expanded samples appears modest. Interestingly, recent studies have implicated SUN1 and LINC complex components as contributors to ALS pathophysiology (Baskerville et al., 2024; Sirtori et al., 2024). Specifically, SUN1 may be a critical mediator of passive permeability of the NPC (Baskerville et al., 2024). Although the mechanisms underlying these events remain unknown, our work suggests that Pan-ExM will likely be a useful tool for providing insight into these neurodegenerative events.

Although one can easily measure NPC diameters in Pan-ExM samples, some caution must be taken when using these measurements to calculate and compare actual NPC diameters across samples as there are no perfect tools for precisely calculating the experimental expansion factor, although the approach we take here suggests that robust reproducibility is possible (Supplementary Figure 1). Regardless, within a single sample one can quantitatively assess relative NPC diameter changes. In this framework, the diameter differences that we observe from evaluating the nuclear ring of the NPC are relatively modest, with NPCs on the bottom versus the top of the nucleus differing by only <10%. However, the quantitative effect on the inner ring is likely more pronounced given prior analysis of how these different elements of the NPC respond to tension (Mosalaganti et al., 2022; Schuller et al., 2021; Zimmerli et al., 2021). We do observe major changes in NPC diameter by Pan-ExM at AL, where the diameters of the NPCs are ~35% more constricted than those at the NE. Thus, we posit that the dimensions of the NPCs in AL reflect a fully constricted state akin to what has been observed for NPC structures in the context of perturbations like energy depletion, hyperosmotic shock, or biochemical fractionation of NEs (Bui et al., 2013; von Appen et al., 2015; Zimmerli et al., 2021). There are several implications of this hypothesis. First, it is likely that LINC-complex dependent mechanotransduction mechanisms only modestly modulate NPC diameter compared to the high variation across the NPC population in an individual nucleus. Second, complete constriction of the NPC likely only occurs under extreme environmental perturbation. In these scenarios, it may be logical for cells to attempt to attenuate nuclear transport by “closing” their NPCs.

Another reason why NPCs may be fully constricted in AL is that they are in an immature state. For example, NPCs in AL have also been suggested to lack key components including the entirety of the nuclear basket (Hampoelz et al., 2016; Hampoelz et al., 2019; Rasala et al., 2008; Walther et al., 2003). The underlying mechanism for why AL NPCs are incompatible with nuclear basket assembly is not understood. One possibility is that, as our data suggest, there are stacking interactions between the outer rings of the NPCs in AL that preclude basket assembly. An alternative model is that basket assembly may only occur in membranes under tension. Such a concept aligns with work exploring the steps in de novo NPC assembly where the basket is curiously added as a terminal step (Onischenko et al., 2020; Otsuka et al., 2023). Further, during post-mitotic NPC assembly early intermediates are assembled into a small nuclear pore before it dilates to complete assembly (Otsuka et al., 2018). More broadly, this interpretation invites the idea that NE tension could directly impact NPC composition. For example, during zebrafish embryonic development NPCs are thought to mature from a constricted state lacking the nuclear basket to a more mature, transport-competent form after the maternal to zygotic transition (Shen et al., 2022). It also has implications for mechanotransduction mechanisms – for example, the local modulation of tension could favor/disfavor the stabile incorporation of nuclear basket proteins, which could direct RNA export, for example, to biochemically polarized NPCs. Our hope is that Pan-ExM will provide a key tool to begin to test these and other hypotheses.

METHODS

Cell culture

HeLa cells were cultured in Dulbecco's modified Eagle medium (DMEM; Gibco, 11965092) supplemented with 10% fetal bovine serum (FBS; Gibco, A5256801), penicillin-streptomycin mix (pen/strep; Gibco, 15140122) and sodium pyruvate (Gibco, 11360070). A549 cells were cultured in DMEM F12 (Gibco, 11320032) with 10% FBS and pen/strep. SH-SY5Y cells were cultured in Eagle's Minimum Essential Medium (EMEM; ATCC, 30-2003) with 15% heat inactivated FBS, pen/strep and 2 mM Glutamax (Gibco, 35050061). iPSCs were grown on Geltrex (Thermo Scientific, A1413302) coated plates and cultured in mTESR1 media (Stem Cell Technologies, 85850). All cells were maintained at 37°C with 5% CO_2. Passaging was performed using 1X PBS and 0.05% Trypsin (Gibco, 25300054) or 0.5 mM EDTA (Corning, 46-034-CI) for iPSCs. 24 h before fixation, ~65,000 cells were seeded onto coverslips coated with 50 µg/mL collagen (Corning, 354236).

Direct-induced motor neuron differentiation

C9orf72 ALS patient and control iPSCs (Supplementary Table 1) were obtained from the Answer ALS repository at Cedars Sinai and differentiated into spinal motor neurons as previously described following a modified direct-induced motor neuron differentiation protocol(Baskerville et al., 2024; Coyne et al., 2020). iPSNs were cryopreserved in Cryostor CS10 media on day 12 of differentiation. Briefly, iPSNs at day 12 of differentiation were thawed and grown on Matrigel (Corning, CLS35623) coated dishes and cultured in stage 3 media composed of 47.5% Iscove's modified Dulbecco's medium (IMDM; Gibco, 12440061), 47.5% F12 (Gibco, 11765054) with 2% B-27 (Gibco, 17504044), 1% MEM Non-Essential Amino Acids (NEAA; Gibco, 11140050), 1% N-2 (Gibco, 17502048), pen/strep, 2.5 µM DAPT (Sigma-Aldrich, D5942), 0.5 µM all-trans retinoic acid (RA; Sigma-Aldrich, R2625), 0.1 µM Compound E (Sigma-Aldrich, 565790) , 0.1 µM dibutyryl-cAMP (Santa Cruz Biotechnology, sc-201567), 0.1 µm SAG (Cayman Chemical Company, 11914), 200 ng/mL Ascorbic acid (Sigma-Aldrich, A4544), 10 ng/mL BDNF (PeproTech, 450-02) and 10 ng/mL GDNF (PeproTech, 450-10). Media was exchanged every 3 days.

CRISPR guide plasmid cloning

Guides targeting *Sun1* and *Sun2* were cloned into the pSpCas9(BB)-2A-Puro (PX459) plasmid (Addgene, 48139) as follows. Primers containing the guide sequences flanked by BbsI (BpiI) cut sites were generated for each gene of interest. Guide sequences for *Sun1* and *Sun2* (Supplementary Table 2) were selected from the Toronto Knockout Library V3(Hart et al., 2017). An additional G nucleotide was added between the BbsI sequence and the guide sequence if the guide sequence did not begin with a G or C. Primers were phosphorylated using a T4 polynucleotide kinase reaction incubated at 37°C for 30 minutes and annealed by bringing the temperature of the reaction from 95°C to 25°C, decreasing by 10°C every minute. The pX459 plasmid was digested using BbsI. The plasmid and guides were annealed using Quick Ligase and transformed into DH5alpha cells. Plasmids were isolated and sequenced to confirm correct guide integration.

***Sun1*$^{-/-}$/*Sun2*$^{-/-}$ double knock-out A549 cell line generation**

All eight guide plasmids (4 for *Sun1* and 4 for *Sun2*) were transfected into A549 cells using the Amaxa Cell Line Nucleofector Kit T (Lonza Bioscience, VCA-1002) according to the manufacturer's instructions and plated into a 10cm plate in A549 media. 48 hours post-transfection, cells were selected using 0.5 µg/mL puromycin in A549 media for 1 week, changing the media every 3 days. After selection, cells were plated at a limiting dilution (0.5 cells / well) into 96-well plates and assessed for colony formation over the following 7-14 days. Wells with single colonies were subsequently expanded and tested for knock-out using a combination of immunofluorescence staining, western blotting, and sequencing (see Supplementary Figure 4).

Cell line validation via gDNA sequencing

Genomic DNA was harvested from clonal cell lines using QuickExtract (Lucigen, QE09050) according to the manufacturer's instructions. Primers were designed to amplify 400 – 600 bp regions containing the guide target site (Supplementary Table 3). Regions of interest were amplified using iProof High-Fidelity DNA polymerase (Bio-rad, 1725301) and sequenced. Sequences were analyzed for the presence of InDels using Synthego ICE analysis (https://ice.synthego.com).

Pan-ExM

Pan-ExM was performed as previously described (M'Saad and Bewersdorf, 2020). Cells were fixed in 4% formaldehyde (FA; Electron Microscopy Sciences, 15710) in 1X PBS for 1 h at RT. Samples were rinsed with 1X PBS three times and post-fixed in 0.7% FA and 1% acrylamide (AAm; Sigma, 01697) in 1X PBS for 6 h at 37°C. Next, samples were washed three times with 1X PBS for 15 min each on a rocking platform and embedded in the first gelling solution (19% sodium acrylate (SA;), 10% AAm, 0.1% N,N′-(1,2-dihydroxyethylene)bisacrylamide (DHEBA; Sigma, 294381), 0.25% Ammonium persulfate (APS; BioRad, 1610700) and 0.25% tetramethylethylenediamine (TEMED; Sigma, T7024) in 1X PBS within custom-constructed gelation chambers for 1.5 h at 37°C in a humidified container. Samples were then incubated in denaturation buffer (200 mM sodium dodecyl sulfate (SDS; Sigma, 75746) , 50 mM tris [hyroxymethyl] aminomethane (Tris; Sigma, T6066), 50 mM sodium chloride (NaCl; JT Baker, 3627-07), pH 6.8 for 15 min at 37°C. Gels were then transferred to 1.5 mL Eppendorf tubes containing denaturation buffer and incubated for 1h at 73°C, then washed three times with 1X PBS for 20 min each on a rocking platform at RT.

For the first expansion, gels were placed in MilliQ water twice for 30 min each then for 1 h. Expanded gels were then incubated in a second gelling solution (10% AAm, 0.05% DHEBA, 0.05% APS and 0.05% TEMED) twice for 20 min each on a rocking platform at RT. After removal of residual solution, gels were sandwiched between a microscope slide and No. 1.5 coverslip, placed in a humidified degassing chamber and perfused with nitrogen gas for 10 min. The chamber was then sealed and incubated for 1.5 h at 37°C.

Next, gels were incubated in a third gelling solution (19% SA, 10% AAm, 0.1% N,N′-methylenebis(acrylamide) (BIS; Sigma, 14602), 0.05% APS and 0.05% TEMED) twice for 15 min each on a rocking platform on ice. After removal of residual solution, gels were sandwiched between a microscope slide and No. 1.5 coverslip, placed in a humidified degassing chamber and perfused with nitrogen gas for 10 min. The chamber was then sealed and incubated for 1.5 h at 37°C. To dissolve DHEBA crosslinks, gels were incubated in 200 mM NaOH (Macron, 7708-10) for 1 h on a

rocking platform at RT. Gels were then washed three times with 1X PBS for 20 min each on a rocking platform at RT.

Immunostaining of Pan-ExM samples

For immunostaining, gels were incubated in primary antibodies (Supplementary Table 4) diluted to 1:500 in antibody dilution buffer (2% bovine serum albumin (BSA; Sigma, A9647) in 1X PBS) for 24 h. Gels were washed three times with PBS-0.1% Tween (PBS-T) for 20 min each, then for 12 h. Next, gels were incubated in secondary antibodies diluted to 1:500 in antibody dilution buffer for 12 h. Gels were washed three times with PBS-T for 20 min each, then for 12 h. All steps were performed on a rocking platform at RT.

Pan-staining and SYTOX Green staining

Gels were incubated in 20 µg/mL NHS ester CF568 (Biotium, 92131) in 100 mM sodium bicarbonate solution (JT Baker, 3506-01) for 1.5 h on a rocking platform at RT. Gels were then washed three times with PBS-T for 20 min each. Next, gels were incubated in SYTOX Green (Thermo Scientific, S7020) diluted to 1:3,000 in calcium and magnesium free HBSS buffer (Gibco, 14170112) for 1 h on a rocking platform at RT. Gels were then washed three times with PBS-T for 20 min each.

Pan-ExM second expansion and sample mounting

Antibody labeled and stained gels were placed in MilliQ water twice for 30 min each then for 1 h. Expanded gels were mounted on 30 mm No. 1.5 glass bottom MatTek dishes with an 18 mm round coverslip on top, and sealed with a two-component silicone (Picodent, 13001000). Samples were then stored in the dark at RT until imaging.

Image acquisition

Data acquisition was carried out on a Dragonfly confocal microscope (Andor) with a water immersion 60x 1.2 NA objective. Fusion software (Andor) was used to control imaging parameters. SYTOX Green, CF568 Succinimidyl ester and ATTO647N were imaged with 488-nm, 561-nm and 647-nm excitation, respectively. Entire cell volumes were acquired by performing z-stack tile scans using a 0.25 µm step size.

Image analysis and visualization

3D reconstruction, volume rendering, and analysis of Pan-ExM images was performed using Imaris versions 9.9-10.2 (Andor). Images and movies were generated using the snapshot and animation tools. Cellular structures were segmented as Imaris Surface, Spot or Cell objects depending on the parameters to be calculated and the object-object statistics to be measured.

Nuclei segmentation

Nuclei were segmented as surface objects by LABKIT machine learning pixel classification of all acquired channels (SYTOX, NHS ester Pan-stain and antibody channels) by manual annotation of foreground and background pixels. A binary mask nucleus channel was then created to account for SYTOX bleaching over large cellular volumes and in stitched images. The masked nucleus channel was used to generate a cell object to measure nuclear volume, surface area, object-orientated bounding box lengths and sphericity.

Total NPC segmentation

To segment all NPCs, regions of interest (ROIs) of a subset of images containing pan-stain and masked nucleus channels were manually annotated in LABKIT. NPC nuclear ring structures were labeled as foreground pixels and iterative training performed until the classifier was able to consistently recognize NPCs in all axial orientations. Performance was assessed by manual inspection of segmentation results and comparing the number of segmented NPCs and number of segmented nup antibody surfaces identified at the NE. To enable quantification of average distances to nearest neighbor objects, a binary mask total NPC channel was created and spot objects with an estimated XY diameter of 0.75 μm (value not corrected for expansion) automatically generated.

NPC diameter segmentation

Given that the total NPC classifier was optimized for robust identification of NPCs across different cells, a separate classifier was trained in LABKIT to accurately measure nuclear ring NPC diameter. ROIs of images containing pan-stain and SYTOX channels were manually annotated, with NPC nuclear ring structures labeled as foreground pixels. Iterative training was conducted until the classifier consistently

segmented the oblate spheroids surfaces corresponding to regions at the NE that were intensely pan-stained and devoid of SYTOX. NPC diameter was quantified as the average of the lengths B and C of the object-orientated bounding box surrounding the segmented nuclear ring NPC surfaces. NPC position at the top or bottom of the nucleus was determined by z-position values.

NPC diameter surface objects were then filtered and split into quintiles based on size. A random 20% of NPC diameter surface objects class was also generated by manual selection of object IDs via a random number generator in Excel. Binary mask NPC diameter channels were created and spot objects with an estimated XY diameter of 0.75 µm (value not corrected for expansion) automatically generated for each NPC diameter class to enable quantification of average distance to nearest neighbor objects. To visualize NPC clustering by size, NPCs were color-coded by NPC diameter class and overlaid on 3D renderings of the nuclear surface. NPC diameter was measured at AL by training a classifier to segment NPC rings visible in top-down view AL stacks on the basis of the pan-stain channel only.

Nup antibody segmentation

Nup antibody signal was automatically segmented in Imaris as surface objects using a background subtraction algorithm and the same manually determined threshold and smoothing settings for each antibody within a set of experiments. Segmented nup antibody surface objects of less than 5 voxels were filtered out. Nup antibody signal was also automatically segmented as spot objects with an estimated XY diameter of 0.75 µm (value not corrected for expansion) and background subtraction selected. Segmentation was performed on entire images to enable identification of antibody distributed at the NE and at AL.

AL segmentation

To segment AL, ROIs of pan-stain channel images were manually annotated in LABKIT and surface objects created by iterative training.

Nup antibody labeling of NPCs analysis

To quantify nup antibody labeling efficiency, the shortest distance from the border of each segmented NPC surfaces to the border of segmented nup antibody surfaces

was computed automatically in Imaris. NPCs were classified as labeled if antibody signal was within 2 μm (value not corrected for expansion).

Nup antibody position analysis

To determine the precise location of nup antibody labeling at NPCs, the shortest distance from the border of the segmented nuclear surface to the center of segmented nup antibody spots was computed automatically in Imaris. Values were normalized to the position of NUP107 to define the 'middle' of NPCs.

Expansion factor measurement

Expansion factors were determined for each experiment by averaging peak-to-peak distances of line profiles drawn through centrioles and mitochondria in expanded samples using the Spots Intensity Profile Imaris XTension in MATLAB (Mathworks). These values were divided by the previously determined dimensions of structures measured by EM to estimate the linear expansion factor.

Statistical analysis

Statistical analyses were performed using Prism 9.4.1 software (GraphPad). Unpaired t-tests, ordinary one-way ANOVA with Tukey's multiple comparisons test or Kruskal-Wallis test with Dunn's multiple comparisons test were used, as denoted in the figure legends, to assess significance, defined as $p<0.05$.

Acknowledgments

We thank Sunandini Chandra for assistance with iPSN cell cultures, Elisa Rodriguez for her invaluable support, and all members of the LusKing laboratory for discussion and feedback. We thank Yuan Tian, Phylicia Kidd and the entire Bewersdorf lab for assistance with Pan-ExM. We thank the ALS patients and their families for essential contributions to this research. This work was funded by the National Institutes of Health R01 NS122236 (to CPL and JDR), F31 HL158119 (to EC), and R01 GM129308 (to MCK).

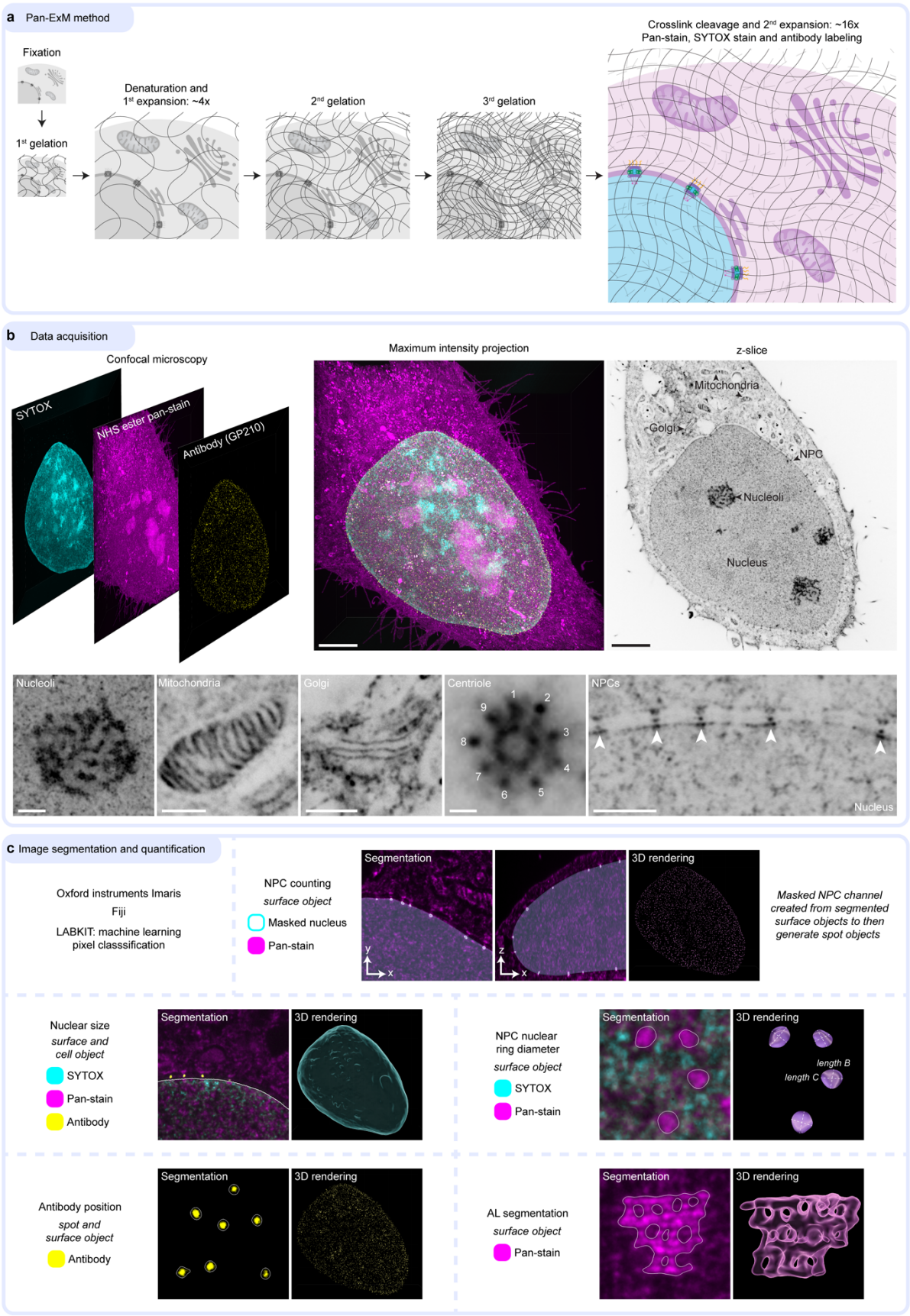

Figure 1. Workflow and image analysis pipeline to visualize and analyze NPCs using Pan-ExM

a. Schematic of the Pan-ExM method adapted from M'Saad and Bewersdorf, 2020. **b.** Overview of Pan-ExM data acquisition by confocal fluorescence microscopy with representative single-channel images of an expanded HeLa cell stained with SYTOX green, NHS ester pan-stain and labeled with an antibody against the nucleoporin GP210. Whole cell volumes can be imaged and visualized as desired - a maximum intensity projection merge and single channel z-slice (inverted) shown as examples. Scale bars 30 µm. The ultrastructure of nucleoli, mitochondria, Golgi stacks, centrioles and NPCs (arrows) are revealed by the pan-stain, shown with an inverted color table. Scale bar 1 µm for centriole panel and 5 µm for all other panels. **c.** Development of image analysis pipelines using Imaris software with the Fiji plugin LABKIT to segment and visualize cellular structures in 3D. Utilizing the denoted image channels and object creation modules (surface, spot and cell) in Imaris; NPCs, nuclei, antibody signal and annulate lamellae (AL) were segmented. Representative images of segmentation results are outlined in single z-slices and 3D renderings are shown.

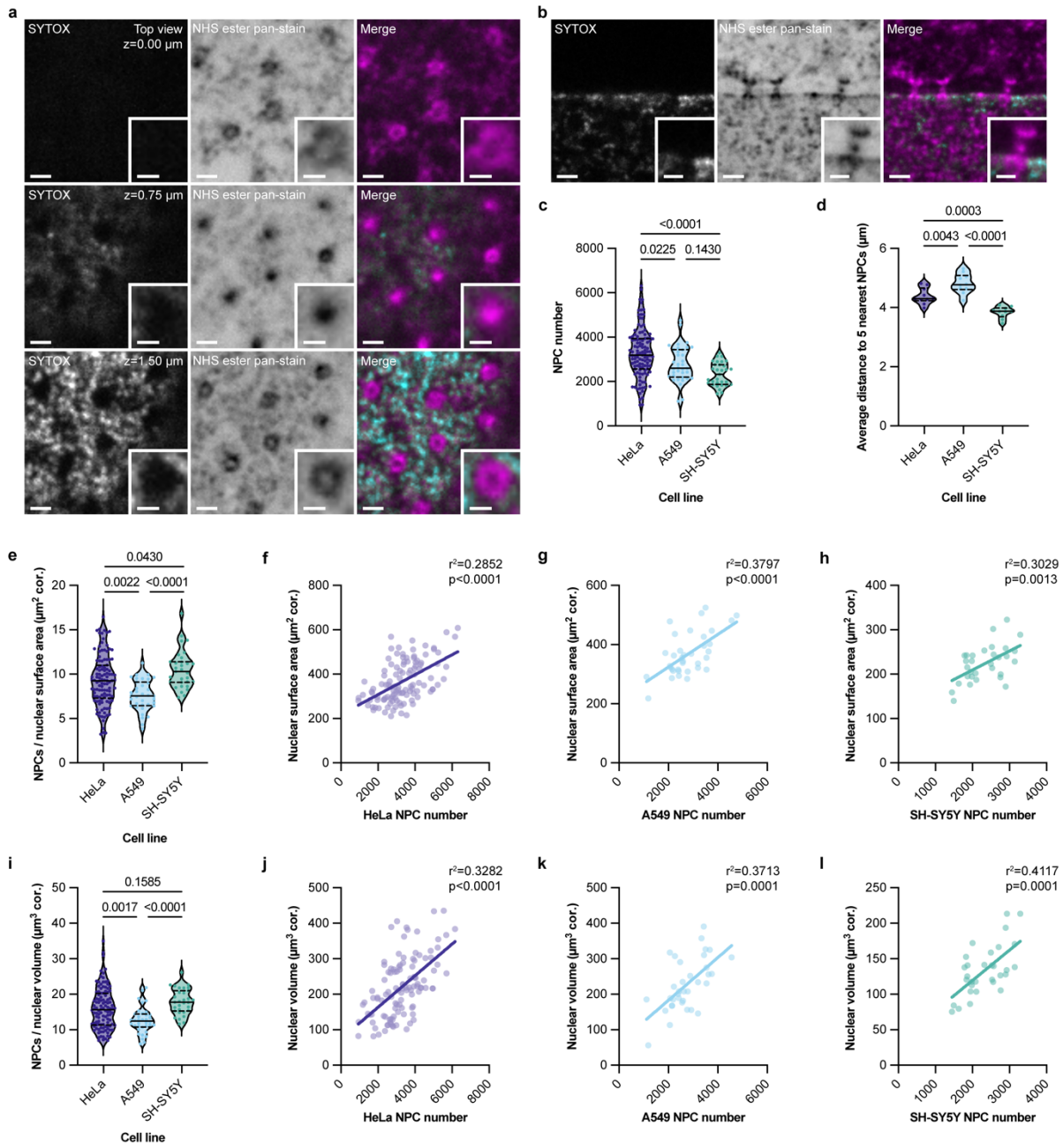

Figure 2. Comprehensive visualization of NPCs with Pan-ExM reveals characteristic NPC density and distribution across representative cell lines

a-b. Representative confocal fluorescence microscopy images of NPCs in expanded HeLa cells stained with SYTOX and NHS ester pan-stain at indicated axial positions (a) and in cross-section (b). Scale bars 2 µm. Insets show magnified view of the NPC, scale bars 1 µm. **c.** Total NPC number is variable and highest in expanded HeLa cells compared to A549 and SH-SY5Y cells. n=31 SH-SY5Y cells from 2 independently expanded samples, n=36 A549 cells from 2 independently expanded samples, n=114 HeLa cells from 4 independently expanded samples. Median values shown as solid lines and quartile values shown as dashed lines. Ordinary one-way

ANOVA with Tukey's multiple comparisons test. **d.** NPCs are most clustered in SH-SY5Y cells. Average distance to the five nearest NPCs measured in cells representative of local NPC density in each cell line. n=10 cells per line. Median values shown as solid lines and quartile values shown as dashed lines. Ordinary one-way ANOVA with Tukey's multiple comparisons test **e.** Overall NPC density (NPCs per nuclear surface area corrected "cor." for the determined expansion factor) is variable across the population but highest in SH-SY5Y cells. Median values shown as solid lines and quartile values shown as dashed lines. Ordinary one-way ANOVA with Tukey's multiple comparisons test. **f-h.** Total NPC number trends with nuclear surface area but with substantial variability. Lines represent a simple linear regression with the coefficient of determination (r^2) indicated. **i.** Total NPC number per nuclear volume (corrected for the determined expansion factor) is more characteristic than NPC density on the nuclear surface. Median values shown as solid lines and quartile values shown as dashed lines. Ordinary one-way ANOVA with Tukey's multiple comparisons test. **j-k.** NPC number generally correlates better with nuclear volume than nuclear surface area (compare to f-h). Lines represent a simple linear regression with the coefficient of determination (r^2) indicated.

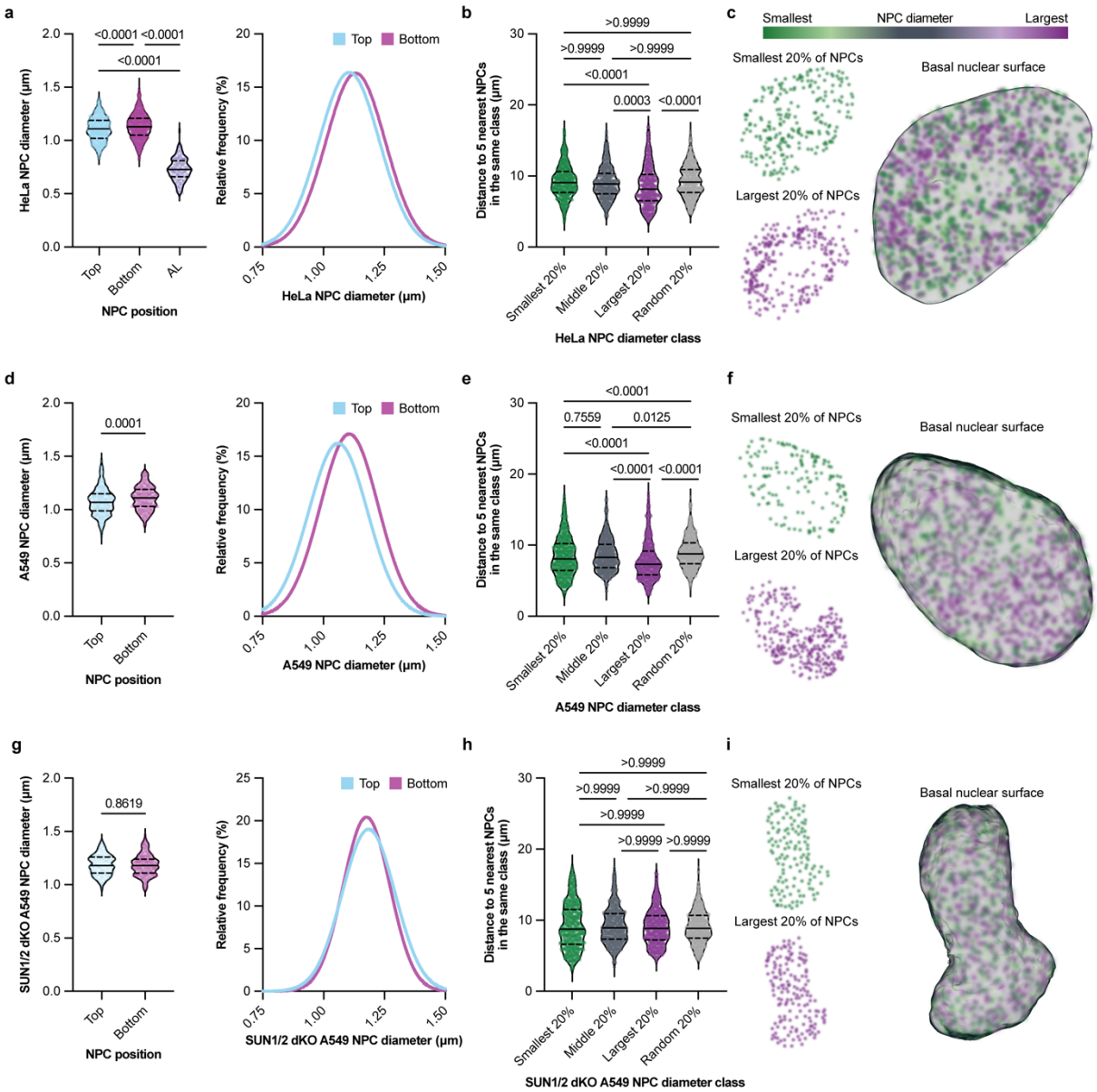

Figure 3. Pan-ExM reveals LINC complex-dependent, local differences in NPC diameter

a. The nuclear ring of NPCs at the bottom (closest to the basal cell surface) of the nucleus are dilated compared to those at the top, but all NE-embedded NPCs are dilated compared to those in AL. Diameter measured at the top and the bottom of the nucleus, and in AL, in HeLa cells. Results also shown as relative frequency distributions with Gaussian curve fitting. n=2335 NPCs in n=10 HeLa cells from a single expansion. **b.** NPCs are more likely to reside near neighboring NPCs of like diameter. Average distance to the five nearest NPCs within the same diameter class in a single HeLa nucleus. n=1984 NPCs. **c.** Visualization of NPC distribution according to dilation state at the basal nuclear surface of a HeLa cell by color-coding

according to NPC diameter class. The most constricted 20% of NPCs are shown in dark green, and the most dilated 20% are shown in dark purple. All NPCs are overlaid on a 3D rendering of the nucleus. **d, e, f.** The same trends in greater NPC dilation on the bottom of the nucleus (n=709 NPCs in n=4 cells from a single expansion) and clustering of NPCs (n=2412) of like diameter is also observed in A549 cells. **g.** Disrupting LINC complexes by CRISPR ablation of *Sun1* and *Sun2* (SUN1/2 dKO) leads to a loss of the bias for greater NPC dilation on the bottom of the nucleus (n=521 NPCs in n=3 SUN1/2 dKO A549 cells from a single expansion). **h, i.** Disrupting LINC complexes leads to homogenization of NPC diameter across the nuclear surface (n=2296 NPCs). For all plots, median values shown as solid lines and quartile values shown as dashed lines. Statistical analysis by ordinary one-way ANOVA with Tukey's multiple comparisons test (a), the Kruskal-Wallis test with Dunn's multiple comparisons test (b, e, h) or unpaired t-test (d, g).

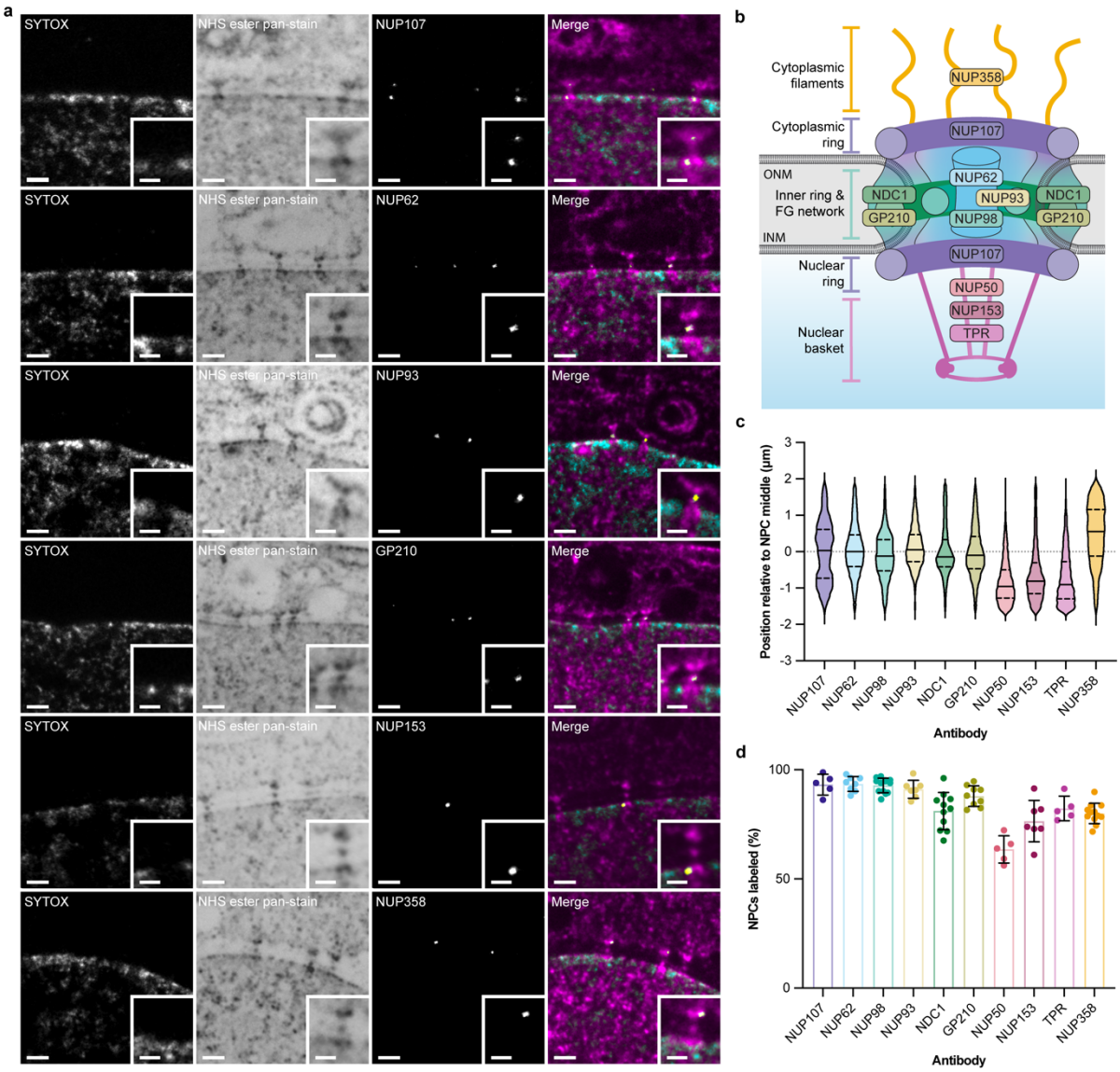

Figure 4. Nup antibody labeling establishes the ability of Pan-ExM to reveal nup position within the NPC ultrastructure

a. Representative confocal fluorescence microscopy images of NPCs in expanded HeLa cells stained with SYTOX, NHS ester pan-stain, and labeled with antibodies against the indicated nups affirms their localization to the expected NPC subunit. Scale bars 2 µm. Insets show a magnified view of the NPC, scale bars 1 µm. **b.** Schematic of the NPC with established nup positions and NPC architectural subunits indicated. ONM: outer nuclear membrane, INM: inner nuclear membrane. **c.** Spatial distribution of nup antibodies along the transport axis in HeLa cells relative to the NPC middle denoted by the dotted line reinforces the ability of PanExM to faithfully retain established NPC architecture. Median values shown as solid lines and quartile values shown as dashed lines. n=2451 segmented NUP107 spots in n=2 cells,

n=9676 segmented NUP62 spots in n=4 cells, n=4083 segmented NUP98 spots in n=2 cells, n=1242 segmented NUP93 spots in n=1 cell, n=13831 segmented NDC1 spots in n=7 cells, n=12213 segmented GP210 spots in n=6 cells, n=2079 segmented NUP50 spots in n=5 cells, n=3988 segmented NUP153 spots in n=4 cells, n=7603 segmented TPR spots in n=5 cells, n=855 segmented NUP358 spots in n=1 cell. Cells from 1-2 independently expanded samples. **d.** Nearly all NPCs segmented based on the NHS ester-pan stain were labeled with antibodies to the inner ring and nuclear/cytoplasmic ring components whereas the peripheral nups were detected at most but not all NPCs. Percentage of NPCs per nuclei labeled with nup antibody in HeLa cells. Bars and error bars are the mean and s.d., respectively. n=82 cells from 4 independently expanded samples.

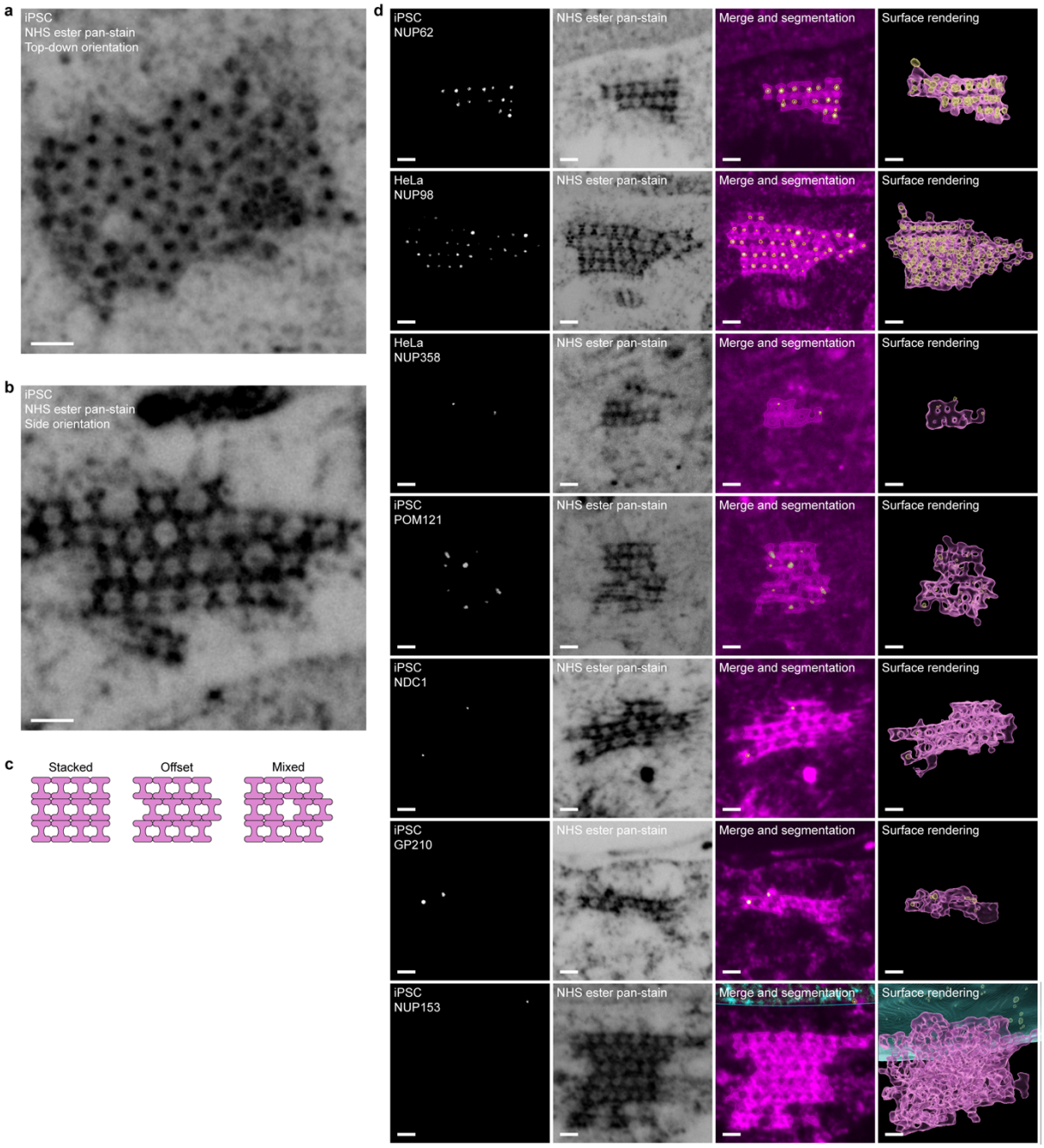

Figure 5. Pan-ExM reveals organization of annulate lamellae

a-b. Stacks of AL – NPCs embedded in the endoplasmic reticulum – can be readily identified by their ultrastructure in Pan-ExM samples. Representative confocal fluorescence microscopy images of AL of expanded iPSCs stained with NHS ester pan-stain in top-down (a) and side view (b) orientations. Scale bars 2 µm. **c.** The organization of individual NPCs in AL ranges from stacked, to offset, or a mixture as illustrated in the schematics. **d.** NPCs in AL are readily stained with antibodies to the FG-nups but are sparsely labeled with antibodies to the transmembrane nups or asymmetric NPC elements. Representative confocal fluorescence microscopy

1 images of AL in expanded iPSC and HeLa cells labeled with antibodies against the
2 indicated nups, and stained with NHS ester pan-stain. 3D surface renderings of
3 segmented structures are also shown. Scale bars 2 μm.
4

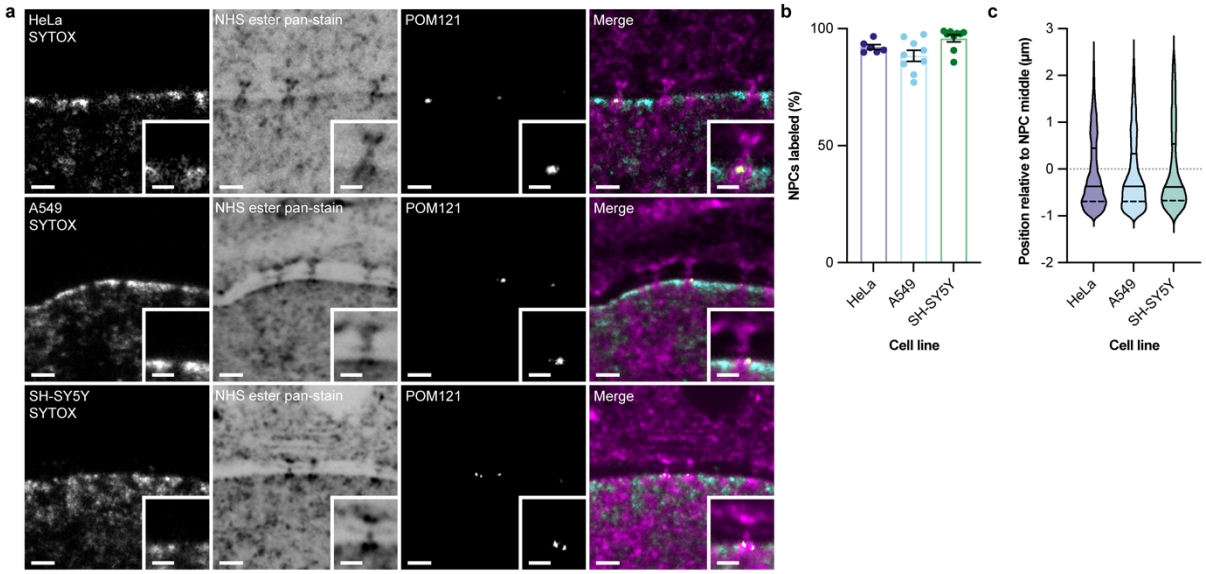

Figure 6. POM121 localizes specifically to the nuclear ring of NPCs

a. POM121 shows a biased distribution towards the nuclear ring of the NPC. Representative confocal fluorescence microscopy images of NPCs in expanded cells of the indicated cell line stained with SYTOX, NHS ester pan-stain, and labeled with an antibody against POM121. Scale bars 2 µm. Insets show a magnified view of the NPC, scale bars 1 µm. **b.** Nearly all segmented NPCs were immunostained with the POM121 antibody. Percentage of NPCs per nuclei labeled with an antibody against POM121 in the indicated cell line. Bars and error bars are the mean and s.d., respectively. n=24 cells from 1-2 independently expanded samples per cell line. **c.** The bias in spatial distribution of POM121 staining at the nuclear ring is observed across the population of NPCs in all cell lines tested. The NPC middle is denoted by the dotted line. Median values shown as solid lines and quartile values shown as dashed lines. n=13831 segmented POM121 spots in n=6 HeLa cells, n=2314 segmented POM121 spots in n=4 SH-SY5Y cells, n=5300 segmented POM121 spots in n=10 A549 cells. Cells from 1-2 independently expanded samples per cell line.

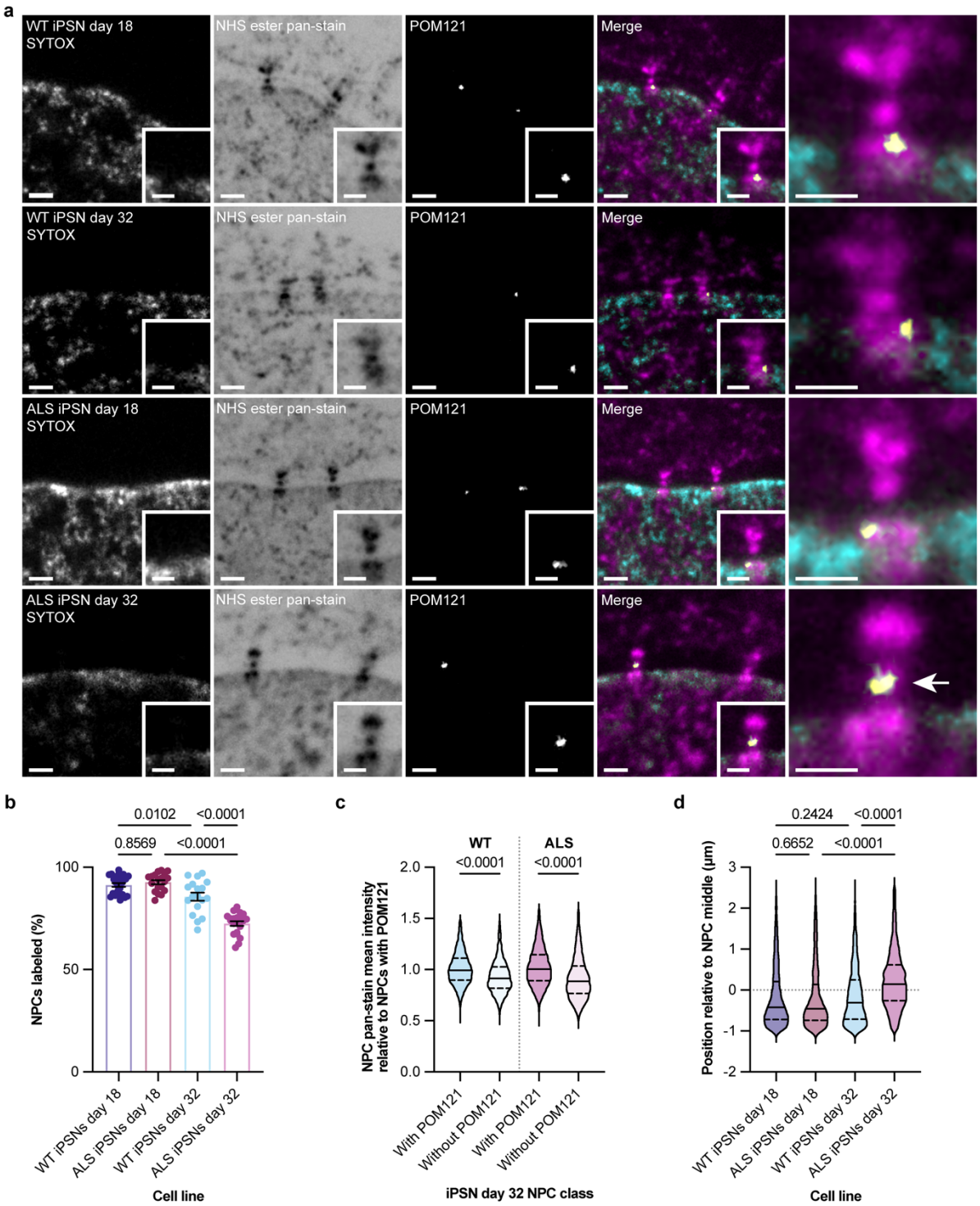

Figure 7. POM121 shifts to the inner ring and is ultimately lost from NPCs in aged model ALS iPSNs

a. POM121 is detected at the inner ring rather than the nuclear ring in “aged” model ALS iPSNs after 32 days of differentiation. Representative confocal fluorescence microscopy images of NPCs in expanded iPSNs derived from a patient with ALS or a matched WT control at indicated number of days after differentiation stained with

SYTOX, NHS ester pan-stain, and labeled with an antibody against POM121. Scale bars 2 μm. Insets and far right panel show magnified views of the NPC, scale bars 1 μm. **b.** The fraction of NPCs labeled with POM121 antibody declines subtly over days of differentiation in WT iPSNs but dramatically in ALS patient-derived iPSNs. Percentage of NPCs per nuclei labeled with an antibody against POM121 in iPSNs of the indicated genotype and number of days after differentiation. Bars and error bars are the mean and s.d., respectively. n=82 cells from 2 independently expanded samples per cell line. Ordinary one-way ANOVA with Tukey's multiple comparisons test. **c.** NPCs lacking POM121 staining have reduced overall pan-stain signal compared to POM121-positive NPCs in the same preparations. Quantification of pan-stain mean intensity at segmented NPCs relative to segmented NPCs with POM121 in iPSNs of the indicated genotype at day 32 post differentiation. n=7215 segmented NPCs in n=8 WT iPSNs day 18 cells, n=2005 segmented NPCs spots in n=8 ALS iPSNs day 18 cells, n=9681 segmented NPCs in n=10 WT iPSNs day 32 cells, n=3146 segmented NPCs in n=10 ALS iPSNs day 32 cells. Each cell line was expanded at the same time. Unpaired t test. **d.** Antibody staining of POM121 is shifted from the nuclear ring to the inner ring across the population of POM121-positive NPCs specifically in "aged" model ALS iPSNs. Spatial distribution of the indicated genotype and number of days after differentiation relative to NPC middle denoted by the dotted line. n=2492 segmented POM121 spots in n=4 WT iPSNs day 18 cells, n=1145 segmented POM121 spots in n=3 ALS iPSNs day 18 cells, n=1647 segmented POM121 spots in n=3 WT iPSNs day 32 cells, n=3093 segmented POM121 spots in n=4 ALS iPSNs day 32 cells. Cells from 2 independently expanded samples per cell line. Median values shown as solid lines and quartile values shown as dashed lines. Kruskal-Wallis test with Dunn's multiple comparisons test.

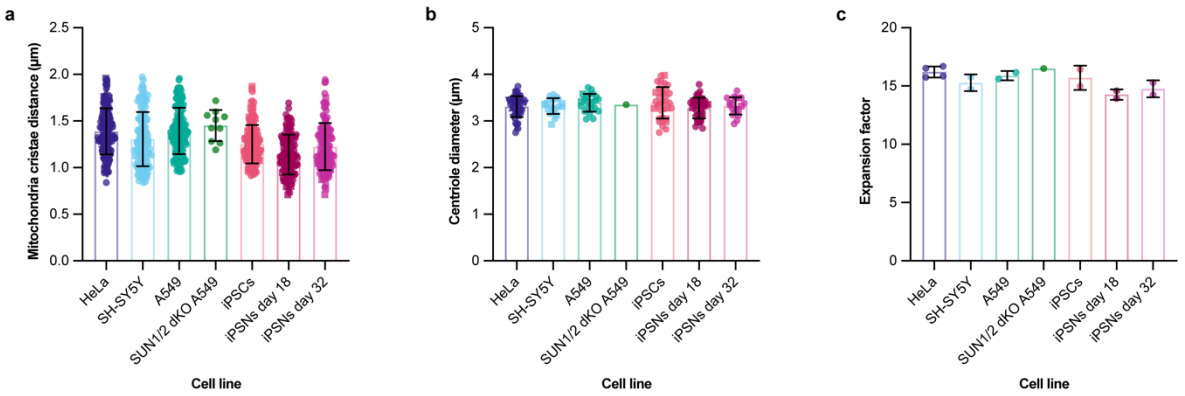

d

Cell line	Expansion experiment	Average mitochondria cristae distance (µm)	Expansion factor assuming the average mitochondria cristae distance is 85 nm	Average centriole diameter (µm)	Expansion factor assuming the average centriole diameter is 210 nm	Average expansion factor
HeLa	1	1.46	17.22	3.39	16.16	16.69
	2	1.49	17.59	3.25	15.46	16.52
	3	1.36	15.99	3.30	15.72	15.86
	4	1.31	15.43	3.37	16.05	15.74
SH-SY5Y	1	1.20	14.16	3.23	15.37	14.76
	2	1.32	15.56	3.36	16.01	15.78
A549	1	1.27	14.94	3.42	16.28	15.61
	2	1.38	16.20	3.38	16.12	16.16
SUN1/2 dKO A549	1	1.45	17.08	3.35	15.94	16.51
iPSCs	1	1.18	13.94	3.40	16.19	15.06
	2	1.38	16.27	3.48	16.59	16.43
iPSNs day 18	1	1.16	13.69	3.25	15.47	14.58
	2	1.02	12.04	3.33	15.84	13.94
iPSNs day 32	1	1.26	14.77	3.32	15.79	15.28
	2	1.07	12.53	3.35	15.97	14.25

Supplementary Figure 1. Approach to define the Pan-ExM expansion factor estimation and correction for each sample

a. Mitochondria cristae distance in expanded samples of the indicated cell lines. n=181 mitochondria in n=31 HeLa cells, n=132 mitochondria in n=27 SH-SY5Y cells, n=154 mitochondria in n=31 A549 cells, n=10 mitochondria in n=2 SUN1/2 dKO A549 cells, n=144 mitochondria in n=30 iPSCs, n=125 mitochondria in n=25 iPSNs day 18 and n=128 mitochondria in n=26 iPSNs day 32. **b.** Centriole diameter in expanded samples of the indicated cell lines. n=50 centrioles in HeLa cells, n=20 in centrioles in SH-SY5Y cells, n=22 centrioles in A549 cells, n=1 centriole in SUN1/2 dKO A549 cells, n=34 centrioles in iPSCs, n=37 centrioles in iPSNs day 18 and n=18 centrioles in iPSNs day 32. Cells from 1-4 independently expanded samples per cell line. **c.** Expansion factors are reproducible across cell lines and experiments. Estimated expansion factors were determined by averaging mitochondrial cristae distance and centriole diameter in cells expanded at the same time. n=15 independent expansion experiments. Bars and error bars are the mean and s.d.,

respectively. **d.** Summary of post-expansion measurements of cellular structures and expansion factor calculations applied in this work.

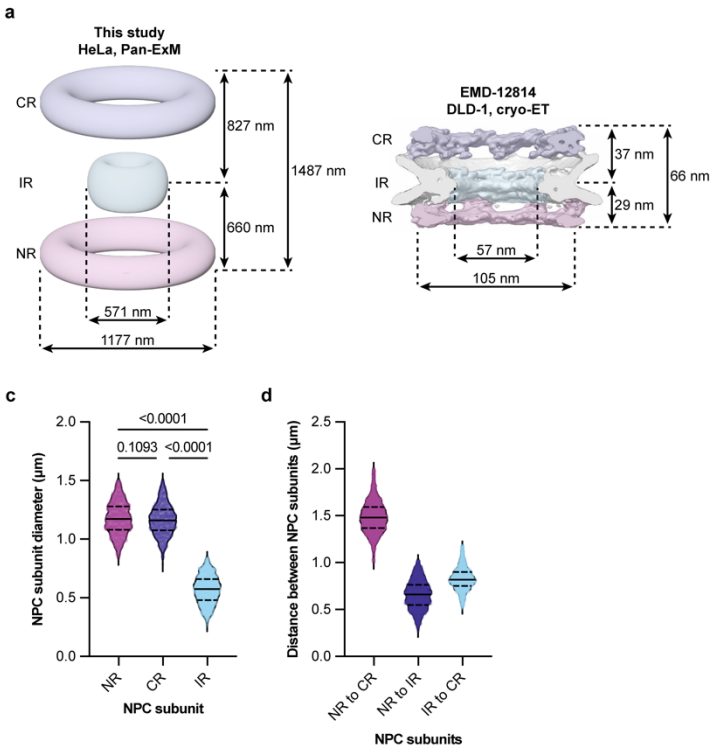

b

Comparison of NPC width ratios

Dimension	Pan-ExM	cryo-ET
NR width	1.00	1.00
IR width	0.51	0.54
NR to CR height	1.33	0.63
NR to IR height	0.74	0.35
CR to IR height	0.59	0.28

Comparison of NPC height ratios

Dimension	Pan-ExM	cryo-ET
NR width	0.75	1.59
IR width	0.38	0.86
NR to CR height	1.00	1.00
NR to IR height	0.56	0.56
CR to IR height	0.44	0.44

Supplementary Figure 2. NPCs in Pan-ExM compared to cryo-ET

a. Average NPC dimensions in expanded samples compared to cryo-ET NPC density map. CR: cytoplasmic ring, IR: inner ring, NR: nuclear ring. **b.** Summary of NPC width and height ratio comparisons in Pan-ExM and cryo-ET samples. **c.** Diameter of the indicated NPC subunits in a Pan-ExM expanded HeLa cell. n=1267 segmented NRs, n=1375 segmented IRs. n=802 segmented CRs. Median values shown as solid lines and quartile values shown as dashed lines. Ordinary one-way ANOVA with Tukey's multiple comparisons test. **d.** Distance between NPC subunits in a Pan-ExM expanded HeLa cell n=2061 segmented NPCs.

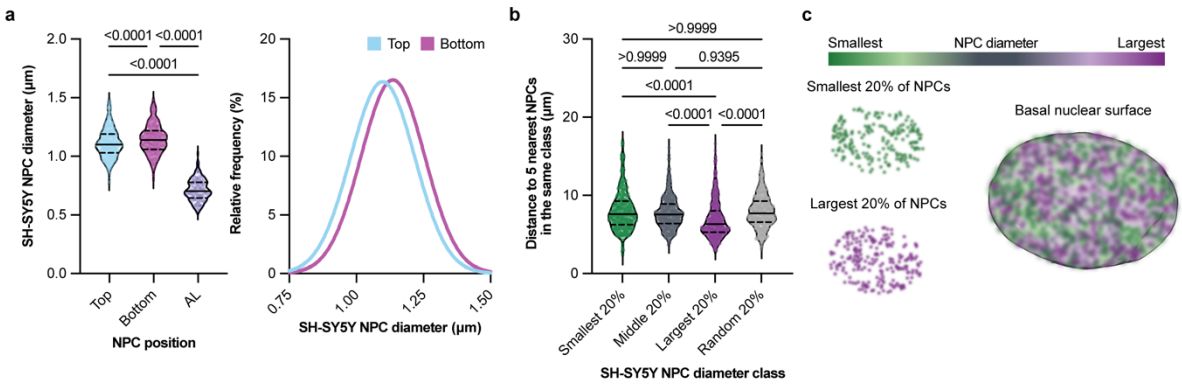

Supplementary Figure 3. Local differences in NPC diameter are also observed in SH-SY5Y cells

a, b. The same trends in greater NPC dilation on the bottom of the nucleus (n=1403 NPCs in n=5 cells from a single expansion) and clustering of NPCs (n=1648) of like diameter described in Figure 3 are also observed in SH-SY5Y cells. Median values shown as solid lines and quartile values shown as dashed lines. Statistical tests: ordinary one-way ANOVA with Tukey's multiple comparisons test (a) and Kruskal-Wallis test with Dunn's multiple comparisons test (b). **c.** Visualization of NPCs at the basal nuclear surface of an SH-SY5Y cell in (b) are color-coded according to NPC diameter class. The smallest 20% of NPCs are shown in dark green, and the largest 20% are shown in dark purple. All NPCs are overlaid on a 3D rendering of the nucleus.

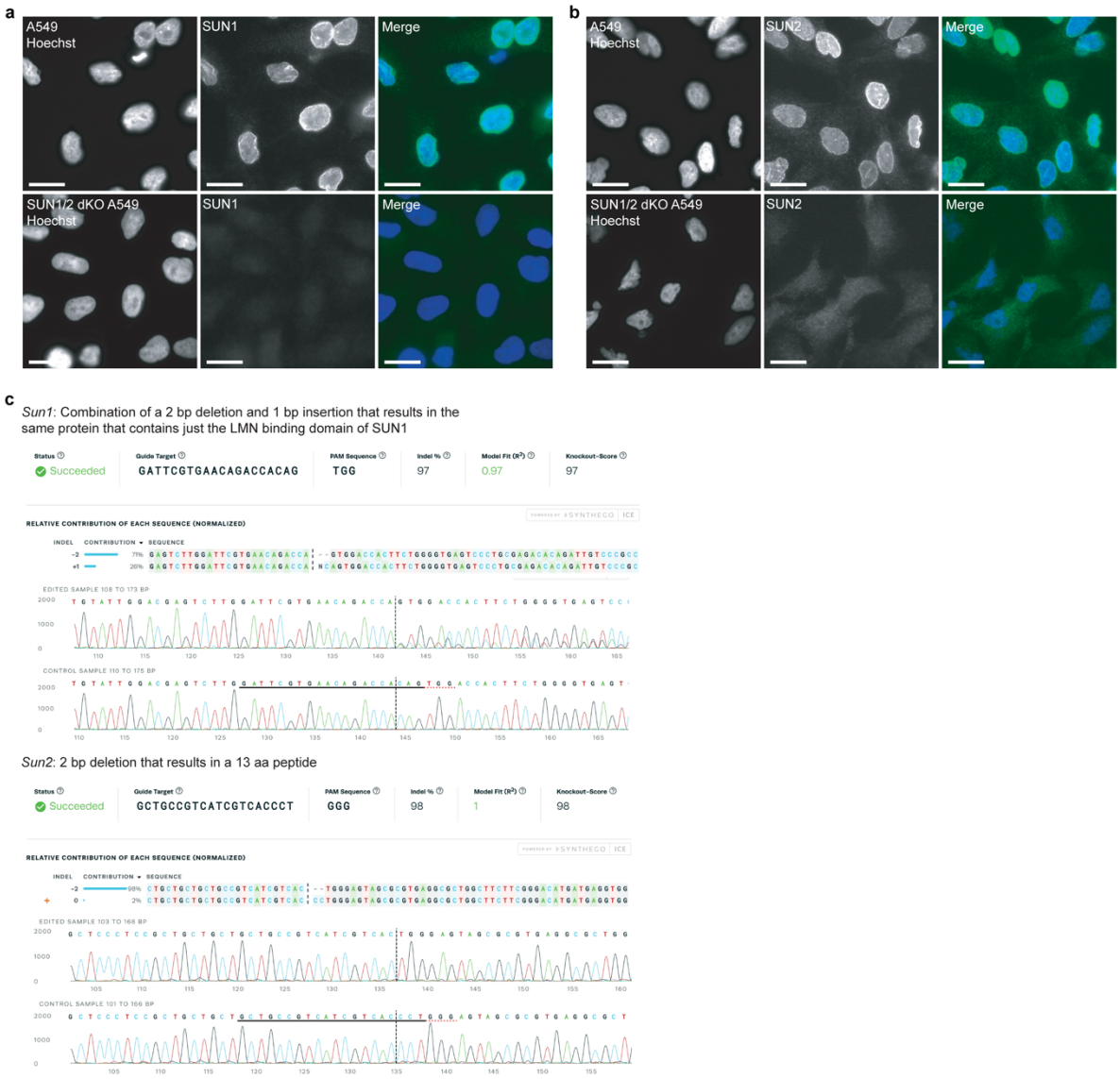

Supplementary Figure 4. Validation of SUN1/2 dKO A549 cell line

a, b. Representative widefield immunofluorescence images of the parental A549 and SUN1/2 dKO A549 cell lines stained with Hoechst (DNA) and immunolabeled with SUN1 (a) or SUN2 (b) primary antibodies and AlexaFluor488-conjugated secondary antibodies, revealing loss of both SUN proteins. Scale bars 20 µm. **c.** Sequencing of PCR-amplified regions containing the target site of the guide RNA demonstrating successful indels incorporated into the coding sequence of *Sun1* and *Sun2*.

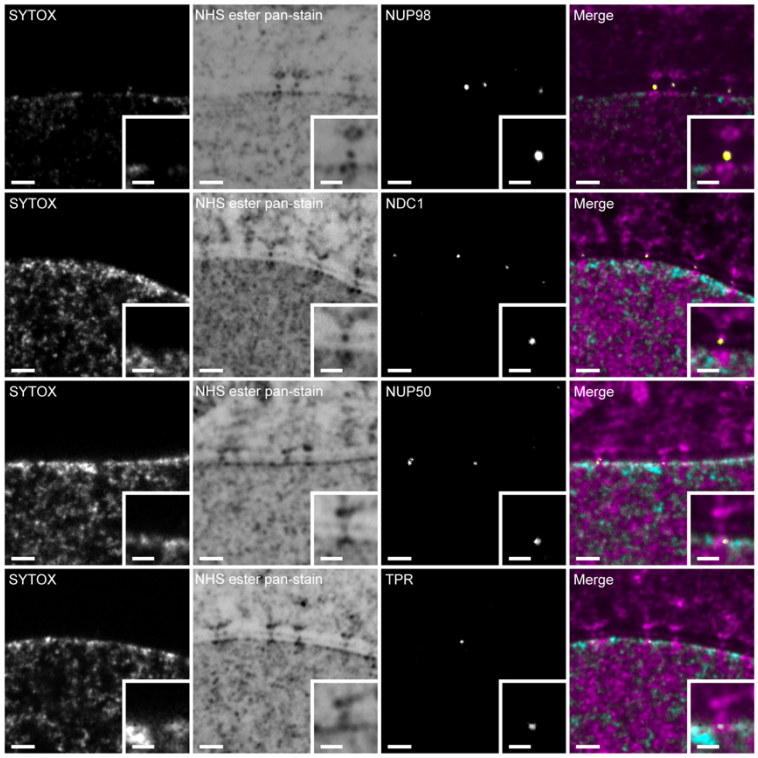

Supplementary Figure 5. Additional nup antibody labeling to support ability of Pan-ExM to reveal Nup position within the NPC ultrastructure

Representative confocal fluorescence images of NPCs in expanded HeLa cells stained with SYTOX, NHS ester pan-stain, and labeled with antibodies against the indicated nups. Scale bars 2 µm. Insets show a magnified view of the NPC, scale bars 1 µm.

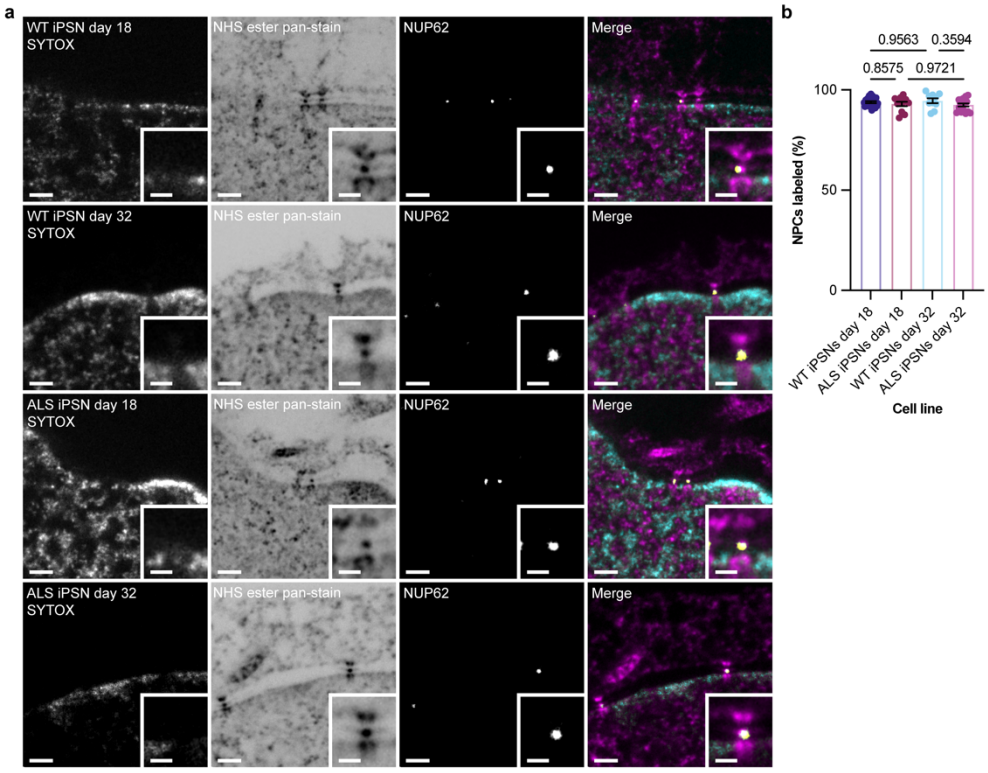

Supplementary Figure 6. Nup62 is retained and its position is unaffected in aged model ALS iPSNs

a. Representative confocal fluorescence microscopy images of NPCs in expanded iPSNs derived from a patient with ALS or a matched WT control at indicated number of days after differentiation stained with SYTOX, NHS ester pan-stain, and labeled with an antibody against NUP62. Scale bars 2 µm. Insets show a magnified view of the NPC, scale bars 1 µm. **b.** Percentage of NPCs per nuclei labeled with an antibody against NUP62 in iPSNs of the indicated genotype and number of days after differentiation. Bars and error bars are the mean and s.d., respectively. n=57 cells from 2 independently expanded samples per cell line. Ordinary one-way ANOVA with Tukey's multiple comparisons test.

References

Akey, C.W., I. Echeverria, C. Ouch, I. Nudelman, Y. Shi, J. Wang, B.T. Chait, A. Sali, J. Fernandez-Martinez, and M.P. Rout. 2023. Implications of a multiscale structure of the yeast nuclear pore complex. *Mol Cell*. 83:3283-3302 e3285.

Akey, C.W., D. Singh, C. Ouch, I. Echeverria, I. Nudelman, J.M. Varberg, Z. Yu, F. Fang, Y. Shi, J. Wang, D. Salzberg, K. Song, C. Xu, J.C. Gumbart, S. Suslov, J. Unruh, S.L. Jaspersen, B.T. Chait, A. Sali, J. Fernandez-Martinez, S.J. Ludtke, E. Villa, and M.P. Rout. 2022. Comprehensive structure and functional adaptations of the yeast nuclear pore complex. *Cell*. 185:361-378.e325.

Arzt, M., J. Deschamps, C. Schmied, T. Pietzsch, D. Schmidt, P. Tomancak, R. Haase, and F. Jug. 2022. LABKIT: Labeling and Segmentation Toolkit for Big Image Data. *Frontiers in Computer Science*. 4.

Baskerville, V., S. Rapuri, E. Mehlhop, and A.N. Coyne. 2024. SUN1 facilitates CHMP7 nuclear influx and injury cascades in sporadic amyotrophic lateral sclerosis. *Brain*. 147:109-121.

Bensidoun, P., T. Reiter, B. Montpetit, D. Zenklusen, and M. Oeffinger. 2022. Nuclear mRNA metabolism drives selective basket assembly on a subset of nuclear pore complexes in budding yeast. *Mol Cell*. 82:3856-3871.e3856.

Bley, C.J., S. Nie, G.W. Mobbs, S. Petrovic, A.T. Gres, X. Liu, S. Mukherjee, S. Harvey, F.M. Huber, D.H. Lin, B. Brown, A.W. Tang, E.J. Rundlet, A.R. Correia, S. Chen, S.G. Regmi, T.A. Stevens, C.A. Jette, M. Dasso, A. Patke, A.F. Palazzo, A.A. Kossiakoff, and A. Hoelz. 2022. Architecture of the cytoplasmic face of the nuclear pore. *Science*. 376:eabm9129.

Bui, K.H., A. von Appen, A.L. DiGuilio, A. Ori, L. Sparks, M.T. Mackmull, T. Bock, W. Hagen, A. Andres-Pons, J.S. Glavy, and M. Beck. 2013. Integrated structural analysis of the human nuclear pore complex scaffold. *Cell*. 155:1233-1243.

Carley, E., R.M. Stewart, A. Zieman, I. Jalilian, D.E. King, A. Zubek, S. Lin, V. Horsley, and M.C. King. 2021. The LINC complex transmits integrin-dependent tension to the nuclear lamina and represses epidermal differentiation. *Elife*. 10.

Chandra, S., and C.P. Lusk. 2022. Emerging Connections between Nuclear Pore Complex Homeostasis and ALS. *Int J Mol Sci*. 23.

Chang, W., H.J. Worman, and G.G. Gundersen. 2015. Accessorizing and anchoring the LINC complex for multifunctionality. *J Cell Biol*. 208:11-22.

Cho, U.H., and M.W. Hetzer. 2020. Nuclear Periphery Takes Center Stage: The Role of Nuclear Pore Complexes in Cell Identity and Aging. *Neuron*. 106:899-911.

Cordes, V.C., S. Reidenbach, and W.W. Franke. 1996. Cytoplasmic annulate lamellae in cultured cells: composition, distribution, and mitotic behavior. *Cell Tissue Res*. 284:177-191.

Coyne, A.N., V. Baskerville, B.L. Zaepfel, D.W. Dickson, F. Rigo, F. Bennett, C.P. Lusk, and J.D. Rothstein. 2021. Nuclear accumulation of CHMP7 initiates nuclear pore complex injury and subsequent TDP-43 dysfunction in sporadic and familial ALS. *Sci Transl Med*. 13.

Coyne, A.N., and J.D. Rothstein. 2021. Nuclear lamina invaginations are not a pathological feature of C9orf72 ALS/FTD. *Acta Neuropathol Commun*. 9:45.

Coyne, A.N., B.L. Zaepfel, L. Hayes, B. Fitchman, Y. Salzberg, E.C. Luo, K. Bowen, H. Trost, S. Aigner, F. Rigo, G.W. Yeo, A. Harel, C.N. Svendsen, D. Sareen, and J.D.

Rothstein. 2020. G(4)C(2) Repeat RNA Initiates a POM121-Mediated Reduction in Specific Nucleoporins in C9orf72 ALS/FTD. *Neuron*. 107:1124-1140.e1111.

Elosegui-Artola, A., I. Andreu, A.E.M. Beedle, A. Lezamiz, M. Uroz, A.J. Kosmalska, R. Oria, J.Z. Kechagia, P. Rico-Lastres, A.L. Le Roux, C.M. Shanahan, X. Trepat, D. Navajas, S. Garcia-Manyes, and P. Roca-Cusachs. 2017. Force Triggers YAP Nuclear Entry by Regulating Transport across Nuclear Pores. *Cell*. 171:1397-1410 e1314.

Feng, Q., M. Saladin, C. Wu, E. Cao, W. Zheng, A. Zhang, P. Bhardwaj, X. Li, Q. Shen, L.E. Kapinos, M. Mariappan, C.P. Lusk, Y. Xiong, R.Y.H. Lim, and C. Lin. 2024. Channel width modulates the permeability of DNA origami based nuclear pore mimics. *bioRxiv*.

Fernandez-Martinez, J., and M.P. Rout. 2021. One Ring to Rule them All? Structural and Functional Diversity in the Nuclear Pore Complex. *Trends Biochem Sci*. 46:595-607.

Fontana, P., Y. Dong, X. Pi, A.B. Tong, C.W. Hecksel, L. Wang, T.-M. Fu, C. Bustamante, and H. Wu. 2022. Structure of cytoplasmic ring of nuclear pore complex by integrative cryo-EM and AlphaFold. *Science*. 376.

Freibaum, B.D., Y. Lu, R. Lopez-Gonzalez, N.C. Kim, S. Almeida, K.H. Lee, N. Badders, M. Valentine, B.L. Miller, P.C. Wong, L. Petrucelli, H.J. Kim, F.B. Gao, and J.P. Taylor. 2015. GGGGCC repeat expansion in C9orf72 compromises nucleocytoplasmic transport. *Nature*. 525:129-133.

Funakoshi, T., M. Clever, A. Watanabe, and N. Imamoto. 2011. Localization of Pom121 to the inner nuclear membrane is required for an early step of interphase nuclear pore complex assembly. *Mol Biol Cell*. 22:1058-1069.

Galy, V., O. Gadal, M. Fromont-Racine, A. Romano, A. Jacquier, and U. Nehrbass. 2004. Nuclear retention of unspliced mRNAs in yeast is mediated by perinuclear Mlp1. *Cell*. 116:63-73.

Hampoelz, B., M.T. Mackmull, P. Machado, P. Ronchi, K.H. Bui, N. Schieber, R. Santarella-Mellwig, A. Necakov, A. Andrés-Pons, J.M. Philippe, T. Lecuit, Y. Schwab, and M. Beck. 2016. Pre-assembled Nuclear Pores Insert into the Nuclear Envelope during Early Development. *Cell*. 166:664-678.

Hampoelz, B., A. Schwarz, P. Ronchi, H. Bragulat-Teixidor, C. Tischer, I. Gaspar, A. Ephrussi, Y. Schwab, and M. Beck. 2019. Nuclear Pores Assemble from Nucleoporin Condensates During Oogenesis. *Cell*. 179:671-686 e617.

Hart, T., A.H.Y. Tong, K. Chan, J. Van Leeuwen, A. Seetharaman, M. Aregger, M. Chandrashekhar, N. Hustedt, S. Seth, A. Noonan, A. Habsid, O. Sizova, L. Nedyalkova, R. Climie, L. Tworzyanski, K. Lawson, M.A. Sartori, S. Alibeh, D. Tieu, S. Masud, P. Mero, A. Weiss, K.R. Brown, M. Usaj, M. Billmann, M. Rahman, M. Constanzo, C.L. Myers, B.J. Andrews, C. Boone, D. Durocher, and J. Moffat. 2017. Evaluation and Design of Genome-Wide CRISPR/SpCas9 Knockout Screens. *G3 (Bethesda)*. 7:2719-2727.

Huang, G., X. Zhan, C. Zeng, K. Liang, X. Zhu, Y. Zhao, P. Wang, Q. Wang, Q. Zhou, Q. Tao, M. Liu, J. Lei, C. Yan, and Y. Shi. 2022a. Cryo-EM structure of the inner ring from the Xenopus laevis nuclear pore complex. *Cell Res*. 32:451-460.

Huang, G., X. Zhan, C. Zeng, X. Zhu, K. Liang, Y. Zhao, P. Wang, Q. Wang, Q. Zhou, Q. Tao, M. Liu, J. Lei, C. Yan, and Y. Shi. 2022b. Cryo-EM structure of the nuclear ring from Xenopus laevis nuclear pore complex. *Cell Res*. 32:349-358.

Ihalainen, T.O., L. Aires, F.A. Herzog, R. Schwartlander, J. Moeller, and V. Vogel. 2015. Differential basal-to-apical accessibility of lamin A/C epitopes in the nuclear lamina regulated by changes in cytoskeletal tension. *Nat Mater*. 14:1252-1261.

Kessel, R.G. 1983. The structure and function of annulate lamellae: porous cytoplasmic and intranuclear membranes. *Int Rev Cytol*. 82:181-303.

King, M.C., C.P. Lusk, and G. Blobel. 2006. Karyopherin-mediated import of integral inner nuclear membrane proteins. *Nature*. 442:1003-1007.

Klughammer, N., A. Barth, M. Dekker, A. Fragasso, P.R. Onck, and C. Dekker. 2024. Diameter dependence of transport through nuclear pore complex mimics studied using optical nanopores. *Elife*. 12.

Kosinski, J., S. Mosalaganti, A. von Appen, R. Teimer, A.L. DiGuilio, W. Wan, K.H. Bui, W.J. Hagen, J.A. Briggs, J.S. Glavy, E. Hurt, and M. Beck. 2016. Molecular architecture of the inner ring scaffold of the human nuclear pore complex. *Science*. 352:363-365.

Kozai, T., J. Fernandez-Martinez, T. van Eeuwen, P. Gallardo, L.E. Kapinos, A. Mazur, W. Zhang, J. Tempkin, R. Panatala, M. Delgado-Izquierdo, B. Raveh, A. Sali, B.T. Chait, L.M. Veenhoff, M.P. Rout, and R.Y.H. Lim. 2023. Dynamic molecular mechanism of the nuclear pore complex permeability barrier. *bioRxiv*.

Krull, S., J. Dorries, B. Boysen, S. Reidenbach, L. Magnius, H. Norder, J. Thyberg, and V.C. Cordes. 2010. Protein Tpr is required for establishing nuclear pore-associated zones of heterochromatin exclusion. *EMBO J*. 29:1659-1673.

Liu, Q., N. Pante, T. Misteli, M. Elsagga, M. Crisp, D. Hodzic, B. Burke, and K.J. Roux. 2007. Functional association of Sun1 with nuclear pore complexes. *J Cell Biol*. 178:785-798.

Lokareddy, R.K., R.A. Hapsari, M. van Rheenen, R.A. Pumroy, A. Bhardwaj, A. Steen, L.M. Veenhoff, and G. Cingolani. 2015. Distinctive Properties of the Nuclear Localization Signals of Inner Nuclear Membrane Proteins Heh1 and Heh2. *Structure*. 23:1305-1316.

M'Saad, O., and J. Bewersdorf. 2020. Light microscopy of proteins in their ultrastructural context. *Nat Commun*. 11:3850.

M'Saad, O., R. Kasula, I. Kondratiuk, P. Kidd, H. Falahati, J.E. Gentile, R.F. Niescier, K. Watters, R.C. Sterner, S. Lee, X. Liu, P. De Camilli, J.E. Rothman, A.J. Koleske, T. Biederer, and J. Bewersdorf. 2022. All-optical visualization of specific molecules in the ultrastructural context of brain tissue. *bioRxiv*.

Megat, S., N. Mora, J. Sanogo, O. Roman, A. Catanese, N.O. Alami, A. Freischmidt, X. Mingaj, H. De Calbiac, F. Muratet, S. Dirrig-Grosch, S. Dieterle, N. Van Bakel, K. Müller, K. Sieverding, J. Weishaupt, P.M. Andersen, M. Weber, C. Neuwirth, M. Margelisch, A. Sommacal, K.R. Van Eijk, J.H. Veldink, G. Lautrette, P. Couratier, A. Camuzat, I. Le Ber, M. Grassano, A. Chio, T. Boeckers, A.C. Ludolph, F. Roselli, D. Yilmazer-Hanke, S. Millecamps, E. Kabashi, E. Storkebaum, C. Sellier, and L. Dupuis. 2023. Integrative genetic analysis illuminates ALS heritability and identifies risk genes. *Nat Commun*. 14:342.

Mitchell, J.M., J. Mansfeld, J. Capitanio, U. Kutay, and R.W. Wozniak. 2010. Pom121 links two essential subcomplexes of the nuclear pore complex core to the membrane. *J Cell Biol*. 191:505-521.

Mosalaganti, S., A. Obarska-Kosinska, M. Siggel, R. Taniguchi, B. Turonova, C.E. Zimmerli, K. Buczak, F.H. Schmidt, E. Margiotta, M.T. Mackmull, W.J.H. Hagen,

G. Hummer, J. Kosinski, and M. Beck. 2022. AI-based structure prediction empowers integrative structural analysis of human nuclear pores. *Science*. 376:eabm9506.

Nino, C.A., D. Guet, A. Gay, S. Brutus, F. Jourquin, S. Mendiratta, J. Salamero, V. Geli, and C. Dargemont. 2016. Posttranslational marks control architectural and functional plasticity of the nuclear pore complex basket. *J Cell Biol*. 212:167-180.

Onischenko, E., E. Noor, J.S. Fischer, L. Gillet, M. Wojtynek, P. Vallotton, and K. Weis. 2020. Maturation Kinetics of a Multiprotein Complex Revealed by Metabolic Labeling. *Cell*. 183:1785-1800 e1726.

Otsuka, S., A.M. Steyer, M. Schorb, J.K. Heriche, M.J. Hossain, S. Sethi, M. Kueblbeck, Y. Schwab, M. Beck, and J. Ellenberg. 2018. Postmitotic nuclear pore assembly proceeds by radial dilation of small membrane openings. *Nat Struct Mol Biol*. 25:21-28.

Otsuka, S., J.O.B. Tempkin, W. Zhang, A.Z. Politi, A. Rybina, M.J. Hossain, M. Kueblbeck, A. Callegari, B. Koch, N.R. Morero, A. Sali, and J. Ellenberg. 2023. A quantitative map of nuclear pore assembly reveals two distinct mechanisms. *Nature*. 613:575-581.

Ou, H.D., S. Phan, T.J. Deerinck, A. Thor, M.H. Ellisman, and C.C. O'Shea. 2017. ChromEMT: Visualizing 3D chromatin structure and compaction in interphase and mitotic cells. *Science*. 357.

Petrovic, S., D. Samanta, T. Perriches, C.J. Bley, K. Thierbach, B. Brown, S. Nie, G.W. Mobbs, T.A. Stevens, X. Liu, G.P. Tomaleri, L. Schaus, and A. Hoelz. 2022. Architecture of the linker-scaffold in the nuclear pore. *Science*. 376:eabm9798.

Rasala, B.A., C. Ramos, A. Harel, and D.J. Forbes. 2008. Capture of AT-rich chromatin by ELYS recruits POM121 and NDC1 to initiate nuclear pore assembly. *Mol Biol Cell*. 19:3982-3996.

Schermelleh, L., P.M. Carlton, S. Haase, L. Shao, L. Winoto, P. Kner, B. Burke, M.C. Cardoso, D.A. Agard, M.G. Gustafsson, H. Leonhardt, and J.W. Sedat. 2008. Subdiffraction multicolor imaging of the nuclear periphery with 3D structured illumination microscopy. *Science*. 320:1332-1336.

Schindelin, J., I. Arganda-Carreras, E. Frise, V. Kaynig, M. Longair, T. Pietzsch, S. Preibisch, C. Rueden, S. Saalfeld, B. Schmid, J.Y. Tinevez, D.J. White, V. Hartenstein, K. Eliceiri, P. Tomancak, and A. Cardona. 2012. Fiji: an open-source platform for biological-image analysis. *Nat Methods*. 9:676-682.

Schuller, A.P., M. Wojtynek, D. Mankus, M. Tatli, R. Kronenberg-Tenga, S.G. Regmi, P.V. Dip, A.K.R. Lytton-Jean, E.J. Brignole, M. Dasso, K. Weis, O. Medalia, and T.U. Schwartz. 2021. The cellular environment shapes the nuclear pore complex architecture. *Nature*. 598:667-671.

Shen, W., B. Gong, C. Xing, L. Zhang, J. Sun, Y. Chen, C. Yang, L. Yan, L. Chen, L. Yao, G. Li, H. Deng, X. Wu, and A. Meng. 2022. Comprehensive maturity of nuclear pore complexes regulates zygotic genome activation. *Cell*. 185:4954-4970 e4920.

Singh, D., N. Soni, J. Hutchings, I. Echeverria, F. Shaikh, M. Duquette, S. Suslov, Z. Li, T. van Eeuwen, K. Molloy, Y. Shi, J. Wang, Q. Guo, B.T. Chait, J. Fernandez-Martinez, M.P. Rout, A. Sali, and E. Villa. 2024. The molecular architecture of the nuclear basket. *Cell*.

Sirtori, R., J.G. M, M.P. E, A. Collins, L. Donatelli, and C. Fallini. 2024. LINC complex alterations are a key feature of sporadic and familial ALS/FTD. *Acta Neuropathol Commun*. 12:69.

Talamas, J.A., and M.W. Hetzer. 2011. POM121 and Sun1 play a role in early steps of interphase NPC assembly. *J Cell Biol*. 194:27-37.

von Appen, A., J. Kosinski, L. Sparks, A. Ori, A.L. DiGuilio, B. Vollmer, M.T. Mackmull, N. Banterle, L. Parca, P. Kastritis, K. Buczak, S. Mosalaganti, W. Hagen, A. Andres-Pons, E.A. Lemke, P. Bork, W. Antonin, J.S. Glavy, K.H. Bui, and M. Beck. 2015. In situ structural analysis of the human nuclear pore complex. *Nature*. 526:140-143.

Walther, T.C., P. Askjaer, M. Gentzel, A. Habermann, G. Griffiths, M. Wilm, I.W. Mattaj, and M. Hetzer. 2003. RanGTP mediates nuclear pore complex assembly. *Nature*. 424:689-694.

Yavuz, S., R. Santarella-Mellwig, B. Koch, A. Jaedicke, I.W. Mattaj, and W. Antonin. 2010. NLS-mediated NPC functions of the nucleoporin Pom121. *FEBS Lett*. 584:3292-3298.

Zhu, X., G. Huang, C. Zeng, X. Zhan, K. Liang, Q. Xu, Y. Zhao, P. Wang, Q. Wang, Q. Zhou, Q. Tao, M. Liu, J. Lei, C. Yan, and Y. Shi. 2022. Structure of the cytoplasmic ring of the Xenopus laevis nuclear pore complex. *Science*. 376:eabl8280.

Zimmerli, C.E., M. Allegretti, V. Rantos, S.K. Goetz, A. Obarska-Kosinska, I. Zagoriy, A. Halavatyi, G. Hummer, J. Mahamid, J. Kosinski, and M. Beck. 2021. Nuclear pores dilate and constrict in cellulo. *Science*. 374:eabd9776.